

RESEARCH PAPER

WiFeS observations of nearby southern Type Ia supernova host galaxies

Anthony Carr,^{1,2} Tamara M. Davis,¹ Ryan Camilleri,¹ Chris Lidman,³ Kenneth C. Freeman,³ and Dan Scolnic⁴

¹School of Mathematics and Physics, University of Queensland, Brisbane, QLD 4072, Australia

²Korea Astronomy and Space Science Institute, Yuseong-gu, Daedeok-daero 776, Daejeon 34055, Republic of Korea

³The Research School of Astronomy and Astrophysics, Australian National University, Stromlo, ACT 2601, Australia

⁴Department of Physics, Duke University, Durham, NC 27708, USA

Author for correspondence: Anthony Carr, Email: anthonycarr@kasi.re.kr.

(Received dd Mmm YYYY; revised dd Mmm YYYY; accepted dd Mmm YYYY; first published online dd Mmm YYYY)

Abstract

We present high-resolution observations of nearby ($z \lesssim 0.1$) galaxies that have hosted Type Ia supernovae to measure systemic spectroscopic redshifts using the Wide Field Spectrograph (WiFeS) instrument on the Australian National University 2.3 m telescope at Siding Spring Observatory. While most of the galaxies targeted have previous spectroscopic redshifts, we provide demonstrably more accurate and precise redshifts with competitive uncertainties, motivated by potential systematic errors that could bias estimates of the Hubble constant (H_0). The WiFeS instrument is remarkably stable; after calibration, the wavelength solution varies by $\lesssim 0.5 \text{ \AA}$ in red and blue with no evidence of a trend over the course of several years. By virtue of the $25 \times 38 \text{ arcsec}$ field of view, we are always able to redshift the galactic core, or the entire galaxy in the cases where its angular extent is smaller than the field of view, reducing any errors due to galaxy rotation. We observed 185 southern SN Ia host galaxies and redshifted each via at least one spatial region of a) the core, and b) the average over the full-field/entire galaxy. Overall, we find stochastic differences between historical redshifts and our measured redshifts on the order of $\lesssim 10^{-3}$ with a mean offset of 4.3×10^{-5} , and normalised median absolute deviation of 1.2×10^{-4} . We show that a systematic redshift offset at this level is not enough to bias cosmology, as H_0 shifts by $+0.1 \text{ km s}^{-1} \text{ Mpc}^{-1}$ when we replace Pantheon+ redshifts with our own, but the occasional large differences are interesting to note.

Keywords: redshift surveys; observational cosmology

1. Introduction

Given that the discrepancy between the Planck 2018 CMB measurement of H_0 , $67.4 \pm 0.5 \text{ km s}^{-1} \text{ Mpc}^{-1}$ (Planck Collaboration et al., 2020) and most recent SH0ES measurement, $73.04 \pm 1.04 \text{ km s}^{-1} \text{ Mpc}^{-1}$ (Riess et al., 2022) is now at the 5σ level, we must ensure we have a comprehensive understanding of any possible systematic errors. In the case of local distance ladder supernova cosmology, these systematics can take many forms when measuring Cepheid/SN brightnesses, recession velocities and distances, and may bias our measurements of cosmic expansion. An extensive set of systematics was recently explored as part of the recent SH0ES/Pantheon+ collaboration (Brout et al., 2022a; Riess et al., 2022, and references therein), including, but not limited to the geometric–Cepheid distance calibration sample (Yuan et al., 2022); the Cepheid–SN calibration sample and Cepheid metallicity dependence (Riess et al., 2022); SN photometry calibration (Brout et al., 2022b); SN dust and colour (Popovic et al., 2021); SN peculiar velocities (Peterson et al., 2022); and SN redshifts (Carr et al., 2022). The general conclusion from these analyses is that SN systematics are not a solution to the Hubble tension, as each individual systematic can only realistically account for a small fraction of the tension, and in fact, often increase the tension.

The most straightforward of the above systematics to test are the SN redshifts. A systematic shift to redshift can easily influence H_0 in much the same way as a systematic shift to measured SN magnitudes, as a magnitude shift is degenerate with a shift in H_0 . A shift in redshift of, e.g. 1×10^{-4} , would be

equivalent to a magnitude shift of around 9 mmag at $z = 0.0233$ and 1.5 mmag at $z = 0.15$. The effect is smaller at higher redshift due to the sub-linear nature of the distance modulus–redshift relation. For the same reason, downward shifts in redshift have a slightly larger effect on magnitude than the same shift upward. According to Davis et al. (2019), redshift errors on the order of only 5×10^{-4} can bias H_0 by nearly $1 \text{ km s}^{-1} \text{ Mpc}^{-1}$, if the errors are systematic and at low- z (the smaller the redshift, the larger the effect). However, in the case of real data, Carr et al. (2022) show that the combined effects of existing redshift and peculiar velocity errors amounted to a negligible shift in H_0 of $-0.12 \pm 0.20 \text{ km s}^{-1} \text{ Mpc}^{-1}$. While this systematic has now been thoroughly ruled out as being a complete solution to the Hubble tension from historical data, there remains a possibility that errors in the measurements of the redshifts are still present.

Carr et al. (2022) used historical data, so here we measure new redshifts to test whether systematics in the historical data are present. Specifically, we target bright, nearby galaxies, which are the most influential to H_0 and have the potential to be biased by, e.g. pointing, where a spectroscopic slit or fibre may be placed not on the core, but elsewhere in the galaxy (such as the location of the supernova). To combat the effects of potential observational bias, we use integral field spectroscopy to ensure we can capture the systemic redshift.

The paper is set out as follows: in Section 2, we detail the target selection, observation and reduction process for our program. In Sections 3 and 4 we detail our analysis of the

calibrations we undertook and the performance of the instrument over the course of our program. Finally, we describe our redshift results compared to historical data and their impact on cosmology in Section 5, and then conclude in Section 6.

2. Observations

We take advantage of integral field spectroscopy to measure the spatial variation in redshift across the face of large galaxies and gather enough signal-to-noise (S/N) to successfully redshift smaller/fainter galaxies. We use the Wide Field Spectrograph (WiFeS) instrument mounted on the Australian National University 2.3 metre telescope (ANU 2.3m) at Siding Spring Observatory (SSO). See [Dopita et al. \(2007\)](#) for the full instrument specifications and [Dopita et al. \(2010\)](#) for the measured performance.

We originally planned to observe using only $R = 7000$ gratings, since these offer higher precision redshifts at the cost of reduced wavelength coverage compared to the $R = 3000$ gratings. The specifications of the grating suite are described in Table 1, and the throughput curves measured by [Dopita et al. \(2010\)](#) are shown in Figure 1. The ANU 2.3m offers full optical spectral coverage at $R = 7000$ over four individual gratings: the ultraviolet and blue gratings are paired with the red and infrared gratings respectively. We opted to use only the B7000+I7000 grating pair as the U7000+R7000 did not offer useful spectral coverage considering observations would take twice as long and add extra overheads swapping grating pairs and beamsplitter.

However, after the first two observing runs, we switched to observing with full spectral coverage at $R = 3000$, which still offers excellent precision and better S/N for the same exposure time. We made this decision due to the fact that at the low redshifts we were targeting, the I7000 grating was sometimes a trade-off between the Calcium triplet and $H\alpha$ region being redshifted out of spectral coverage. We show this in Figure 1 with two example spectra at redshifts where the I7000 spectral region would be devoid of features. If we have good enough S/N for a late-type galaxy, or the galaxy has a particularly strong Calcium triplet, we would still be able to identify features in I7000 below $z \approx 0.014$, and similar for early-type galaxies above $z \approx 0.065$. However, for the final two observation runs, we observed using the B3000+R3000 gratings since they offer full spectral coverage with a generous overlap, and as such have no such restrictions on where typical optical galaxy emission and absorption features land.

2.1 Target Selection

The catalogue was created using the Pantheon supernova sample ([Scolnic et al., 2018](#)) since we conducted all of our observations before the release of Pantheon+. Galaxies were chosen to be easily observable from Siding Spring Observatory (latitude 149.06° , longitude -31.27°), i.e. airmass $\lesssim 1.5$, and with $z \lesssim 0.1$ as these are the redshifts most influential to H_0 . The strategy was to observe in Nod&Shuffle mode, which results in simultaneous science and sky spectra. The target is exposed on the science CCD pixels, then the telescope is nodded to

Table 1. WiFeS grating wavelength ranges and dispersion, as measured from our reduced data. Wavelength limits are rounded to the nearest 5 Å. The beamsplitters are named after their dichroic wavelength split in nanometres. The dispersion and upper wavelength limit for each grating varied over time by less than 0.02%.

Grating	Beamsplitter	λ_{\min} Å	λ_{\max} Å	Dispersion Å/pixel
U7000	RT480	3290	4355	0.272
B7000	RT615	4180	5550	0.347
R7000	RT480	5290	7025	0.439
I7000	RT615	6830	9055	0.566
B3000	RT560	3200	5900	0.775
R3000	RT560	5300	9565	1.25

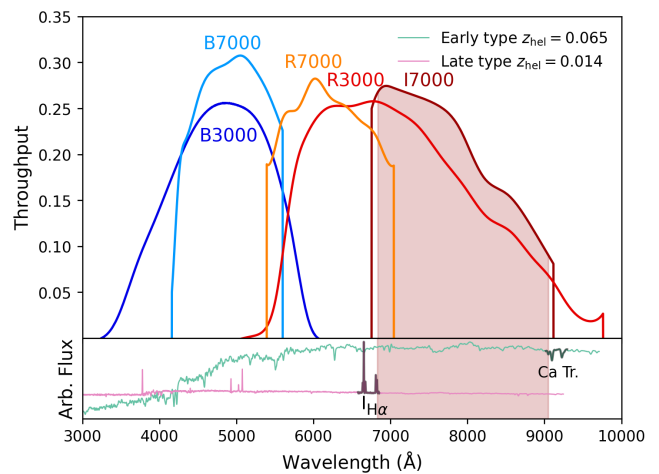


Figure 1. Measured throughput of each grating except for U7000 from [Dopita et al. \(2010\)](#). The shaded region represents the I7000 wavelength bounds in practice (Table 1). The bottom panel shows two examples of spectra that might fail to be redshifted from the I7000 grating. For a redshift of $\lesssim 0.014$ ($\gtrsim 0.065$), none of the $H\alpha$ (Calcium triplet) region is present in I7000 leaving only weak or no features.

empty sky and the charge already present is ‘shuffled’ across the CCD so that the sky is exposed on a different set of pixels. Sky subtraction is then just the simple case of subtracting the pure 2D sky spectrum from the observed object+sky 2D spectrum within the same CCD image during data reduction, leaving just the 2D object spectrum. Each galaxy observation was made up of three Nod&Shuffle cycles, with each sky and object exposure being the same length. The sky field was chosen to be as empty as possible, and close by to reduce the time to nod between frames.

Once the targets were chosen, we calculated the rough exposure time using the WiFeS performance calculator.^a The aim was a generous S/N of at least 20 in the blue camera after the full $3 \times$ Nod&Shuffle cycle, which was easily obtained for the brightest galaxies. The red camera naturally gathers more signal for the same observation time, so observation time was optimised for the blue camera. Exposure time depends on the moon phase (all observations were done in grey or dark time), the seeing full width at half maximum (FWHM; typically 1.6

^a<https://www.mso.anu.edu.au/rsaa/observing/wifes/performance.shtml>

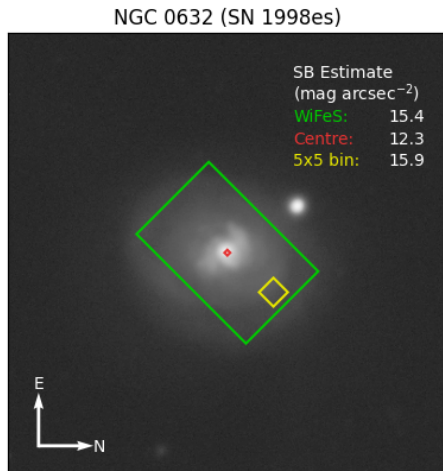


Figure 2. DECam g-band image of the galaxy NGC 632, host of SN 1998es. The three estimates of surface brightness were made over the whole WiFeS aperture, within the central pixel of the aperture, and finally, a 5x5 pixel binned aperture on the outskirts to estimate a lower limit of surface brightness.

arcsec at SSO), as well as the airmass and surface brightness of the target. The average total integration time was 485 s for an estimated average g-band surface brightness of 16 mag arcsec⁻². Subexposure times were rounded to the nearest 30 seconds rather than attempting to save small amounts of time optimising to the nearest second.

Surface brightness was estimated directly from Dark Energy Camera (DECam) images using the US National Science Foundation’s NOIRLab Astro Data Lab image cutout service.^b Most targets had images; for those that did not, we estimated surface brightness by comparison with similar targets that did have images. When there were images, we opted for sky-subtracted images in the g-band as the highest priority, followed by r-band then i-band (with minor corrections to account for overestimating the g-band magnitude), and stacked images if no sky-subtracted version was available. The surface brightness was estimated from the images using the `photutils` python package^c within different apertures, including the full WiFeS aperture, to estimate a useful average for the whole field of view. See Figure 2 for an example.

Flux calibration stars were chosen to be CALSPEC stars^d which are the standards used for the Hubble Space Telescope. The only criterion for choosing a CALSPEC flux calibrator was that it was easily observable from SSO. The CALSPEC standard stars were also used to remove Telluric absorption features from the galaxy spectra. We trialled the use of dedicated, particularly smooth-spectrum Telluric standard stars (host, main sequence B stars), but were unable to reliably source reference spectra. As such, the Telluric corrections were sometimes lacking, but never resulted in a failure to compute a redshift.

^b<https://datalab.noirlab.edu/sia.php>

^c<https://photutils.readthedocs.io/en/stable/>

^d<https://www.stsci.edu/hst/instrumentation/reference-data-for-calibration-and-tools/astronomical-catalogs/calspec>

Radial velocity standard stars (stars with well-known radial velocities to compare to as another form of instrument calibration) were chosen from Nidever et al. (2002). The stars we used were all chosen to be G- or K-type stars with a preference for giants. They were also chosen to primarily be around $V = 6$ mag, similar to the flux calibrators.

2.2 Reduction

We used version 0.7.4 of the default WiFeS reduction pipeline, PyWiFeS (Childress et al., 2014), to transform the raw observations into calibrated, 3D data cubes. In brief, the reduction pipeline pre-processes each CCD image (overscan and bias subtraction, bad pixel repair), then uses spatial calibration frames to split the data into the 25 science and 25 sky slitlets. The instrument was designed so that the sky and science slitlets are interleaved on the detectors, and slitlets lie along detector rows. Over the entire detector, the slitlets deviate from these rows by up to $\sim \pm 0.5$ pixels. This deviation is accounted for by observing a uniformly illuminated calibration frame obstructed by a straight wire. The shadow of the wire is used to find the spatial zero-point of each slitlet along the y -direction (the long axis of the aperture) over every CCD column.

From here, the usual steps are performed: finding the wavelength solution, cosmic ray rejection, sky-subtraction, flatfielding, flux calibration and Telluric correction. Finally, the data are reformatted to a 3D data cube. We note that while the field of view is 25×38 arcsec, in practice we trim the noise-dominated outer one or two spaxel rows (depending on the gratings and beamsplitter) so we actually use 25×35 spaxels for our purposes.

Due to the excellent stability of the WiFeS instrument, the wavelength solution varied only on the sub-pixel level. We expand upon this in Section 3.

2.3 Spaxel binning and redshifting

After reducing the data, the 3D spectral data cube contains a wealth of information. For this work, we are mainly interested in the redshift and its spatial dependence, although there is certainly more that can be done with spatially varying, medium-resolution ($R = 3000\text{--}7000$), high S/N data. To investigate the redshift(s) of the galaxy, we first processed the data further into a format that could be ingested into the Marz redshifting tool,^e which was developed primarily for the use of the Australian Dark Energy Survey and Anglo-Australian Telescope, also at SSO. This included Voronoi binning the spaxels using the `vorbin` python package (see Cappellari & Copin, 2003) to gather signal in the outer regions of the aperture, and to successfully redshift the galaxies that occupied very few spaxels.

See Figure 3 for a visualisation of how observations are turned into redshifts. It shows the case of a galaxy larger than the aperture, where spaxels further from the bright central region are binned to a common S/N threshold. Each Voronoi

^e<https://samreay.github.io/Marz>. The default tool does not include the calcium triplet, so we modified the source code for our own use.

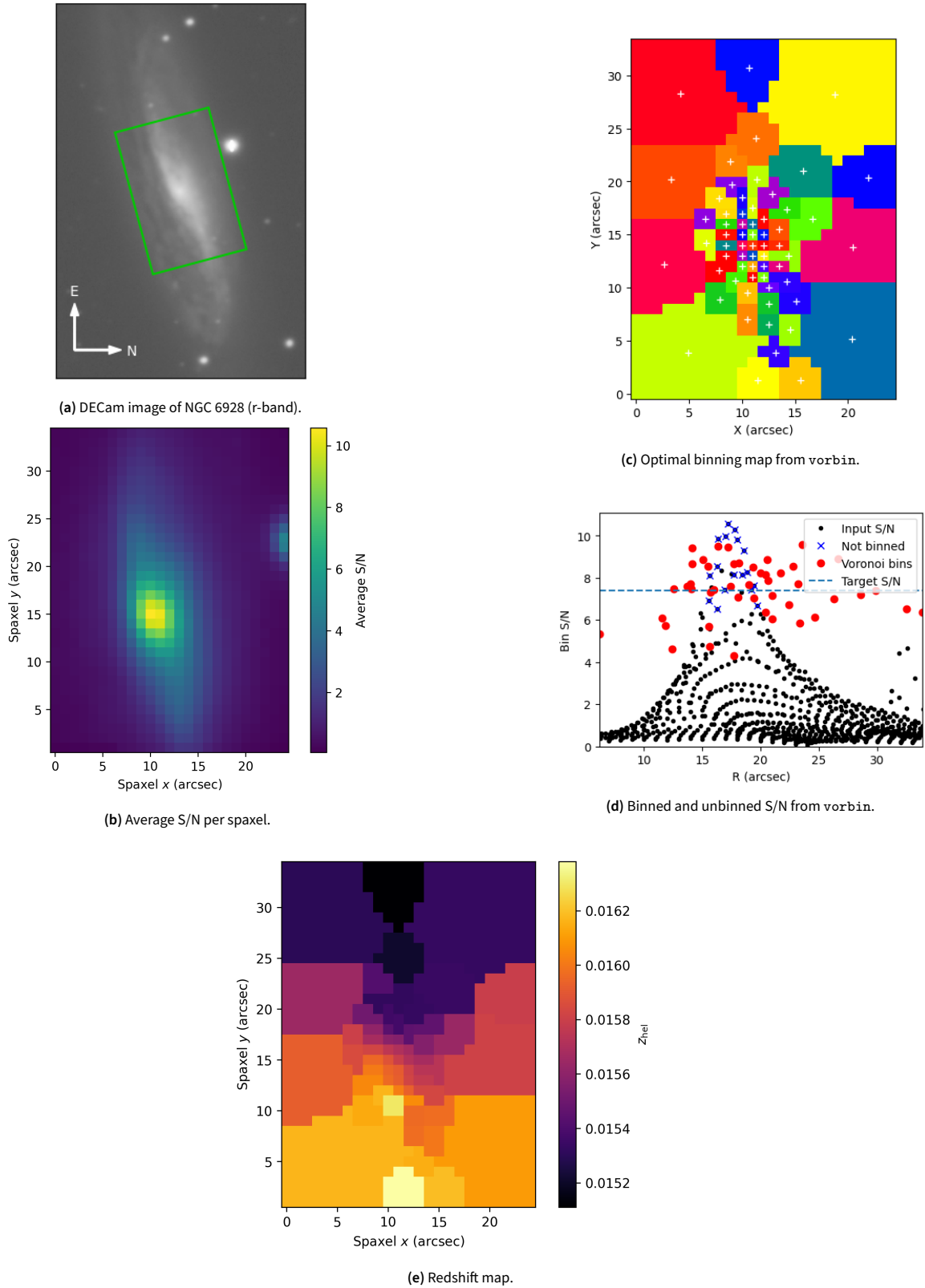


Figure 3. **a)** Image of NGC 6928 on the sky with the WiFeS field of view in green. SN 2004eo occurred outside the green aperture pictured here, nearly one arcminute east-north-east of the centre of the galaxy. **b)** S/N over the WiFeS aperture, as averaged per spaxel over the entire red camera spectra. Evidence of the nearby star can be seen as an increase in S/N around spaxel coordinates (25,23), ~ 35 arcsec from spaxel (0,0). **c)** The Voronoi binning regime that results in each bin having roughly 70% the average S/N of the central spaxel, with the dashed line showing the S/N target. **d)** The S/N of each unbinned and binned spaxel, with the dashed line showing the S/N target. **e)** Final redshift map, showing rotation along the long axis. The average redshift of all the spaxel bins is $z_{\text{hel}} = 0.01576$, with standard deviation 2.9×10^{-4} .

bin is then redshifted separately. From this map, the average redshift of the whole galaxy, the redshift of the centre and the redshift in the locality of the SN can all be found. The particular example shown does not contain the SN in the aperture; there is only a moderate probability of the SN being within the field of view when centred on such large galaxies.

For most of the Voronoi binning, we set the S/N target to 90% of the central pixel S/N by default. This target level was sometimes adjusted in the cases where the surface brightness profile was particularly flat (requiring an increase), such as MCG-02-02-086, the host of SN 2003ic, or the galaxy as a whole was extremely bright (requiring a decrease to reduce the number of bins from ≥ 100 to $\lesssim 100$), such as NGC 6928, featured in Figure 3. In each case, the binning was visually inspected to ensure both a decent number of bins and high-quality spectra for each.

In 24 cases, there was only one bin, necessary for the particularly small/faint/poor-quality-spectrum galaxies to successfully obtain an accurate redshift. Where possible, we also redshift just the central region (estimated from the highest S/N spaxels), to compare with the average redshift over all Voronoi bins. This often resulted in a strong increase in S/N; however, for the 24 cases above, a similar or lower S/N spec-

trum naturally resulted, since we did not use as many spaxels as for the whole galaxy. Of the 185 galaxies we observed, 106 were at least roughly as large in the sky as the aperture, and nine were small enough to occupy only several spaxels each. For the standard stars, the 3×3 spaxel region around the centre of the star was used for redshifting.

The geocentric-to-heliocentric correction to account for our motion around the Sun is automatically handled in Marz by including the relevant headers for the telescope location, observation time and object coordinates. The distribution of geocentric corrections between -25 km s^{-1} and $+20 \text{ km s}^{-1}$ only had a slight positive gradient; however, the mean correction was 11.7 km s^{-1} due to a large number of corrections falling between $+20 \text{ km s}^{-1}$ and $+30 \text{ km s}^{-1}$.

3. Instrument throughput correction

Transforming the data from photon counts to accurate flux as a function of accurate wavelength is a multi-step process. ‘Dome’ flats using an internal Quartz-Iodine lamp correct for the CCD pixel-to-pixel quantum efficiency. The Quartz-Iodine lamp is mostly ‘spectrally flat’, in that the wavelength dependence can be removed by a moderate order polynomial,

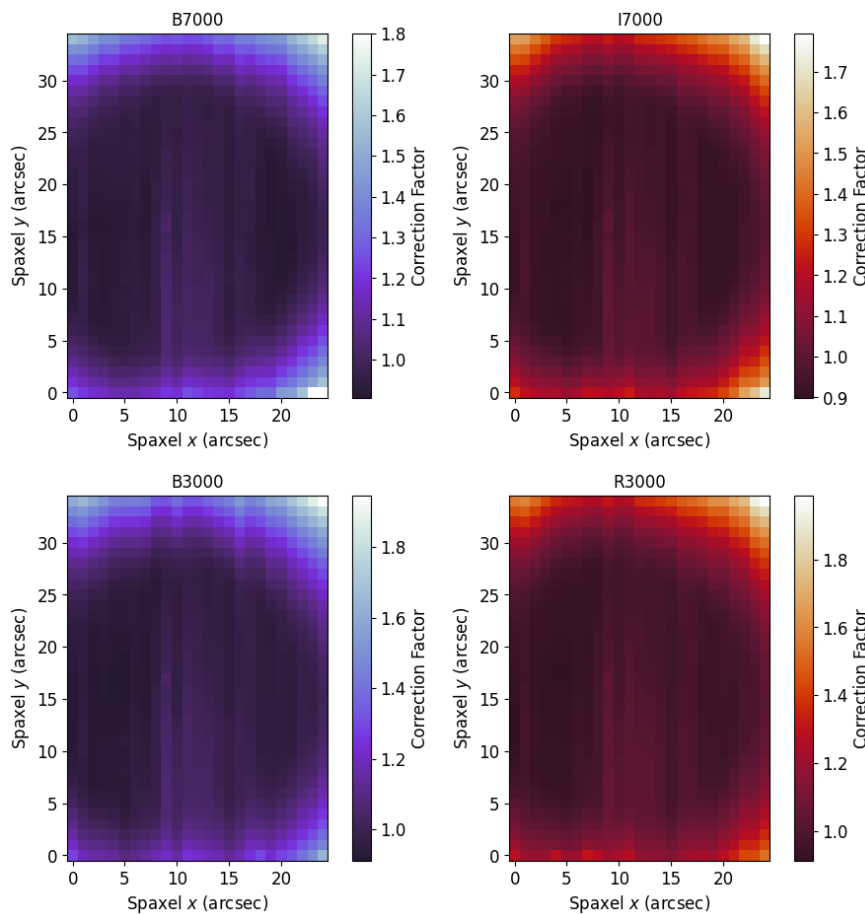


Figure 4. Illumination corrections for the red and blue camera averaged over each observation run in each operation mode. The $R = 3000$ and $R = 7000$ grating corrections are basically the same since this is a spatial correction. The corrections are also comparable to those of Childress et al. (2016) indicating the stability of the instrument over several years.

but does not illuminate the instrument perfectly uniformly. Twilight flats using the twilight sky (which are ‘spatially’ flat, i.e. uniform illumination, but significant spectral deviation) are used to correct for the spatial illumination. Once the pixel-to-pixel and large-scale illumination are corrected, one of the final steps is flux calibration, which corrects for the wavelength response and instrument+atmosphere throughput.

Childress *et al.* (2016) studied the performance of the WiFeS instrument over a three-year period for the ANU WiFeS SuperNova Programme (AWSNAP), including wavelength solution, illumination correction, and flux calibration. We have a similar set of data gathered over a year in two operation modes, five years later, with which to compare. We emulate their analysis here to observe any trends over nightly to yearly scales and detect any need for manual recalibration. We start by examining the illumination correction for our different operating modes (see Figure 4), and find no significant differences (visually) between them and Childress *et al.* (2016), which speaks to the stability of the instrument.

4. Wavelength calibration methods

It is well known that temperature fluctuations inside the dome affect the wavelength solution of WiFeS spectra, as the gratings themselves thermally expand. We endeavoured to mitigate any temperature effects by taking frequent arc lamp calibration frames. The response of the gratings to temperature fluctu-

ations may be linear, which can be interpolated over easily, but the temperature fluctuations themselves are not and lag behind the dome internal temperature readings. By making frequent arc lamp observations, temperature variations are accounted for since each science observation is calibrated using the nearest arc lamp in time (or if the science observation falls between two arc lamps, it is calibrated by the average of those wavelength solutions). We track the wavelength solution over the course of each night and over the entire observation program, which we detail in this section. In essence, we find that the wavelength solution shows excellent stability and thus our redshifts require no spatial or temperature correction.

4.1 Arc lamp wavelength solutions and temperature dependence

Similar to Childress *et al.* (2016), we investigated the variation of the wavelength solution over the CCD, and over time, and we compare both of these to dome temperature readings to correlate with the fluctuations.

Figures 5–7 show our investigation into wavelength solution variation as measured from arc lamp observations. Over our entire observation program that spanned one year, we used two different resolutions each for two runs (approximately spanning 6 months each). We find very similar results to Childress *et al.* (2016), in that the average wavelength solution generally deviates by $\pm 0.5 \text{ \AA}$ which for our gratings is

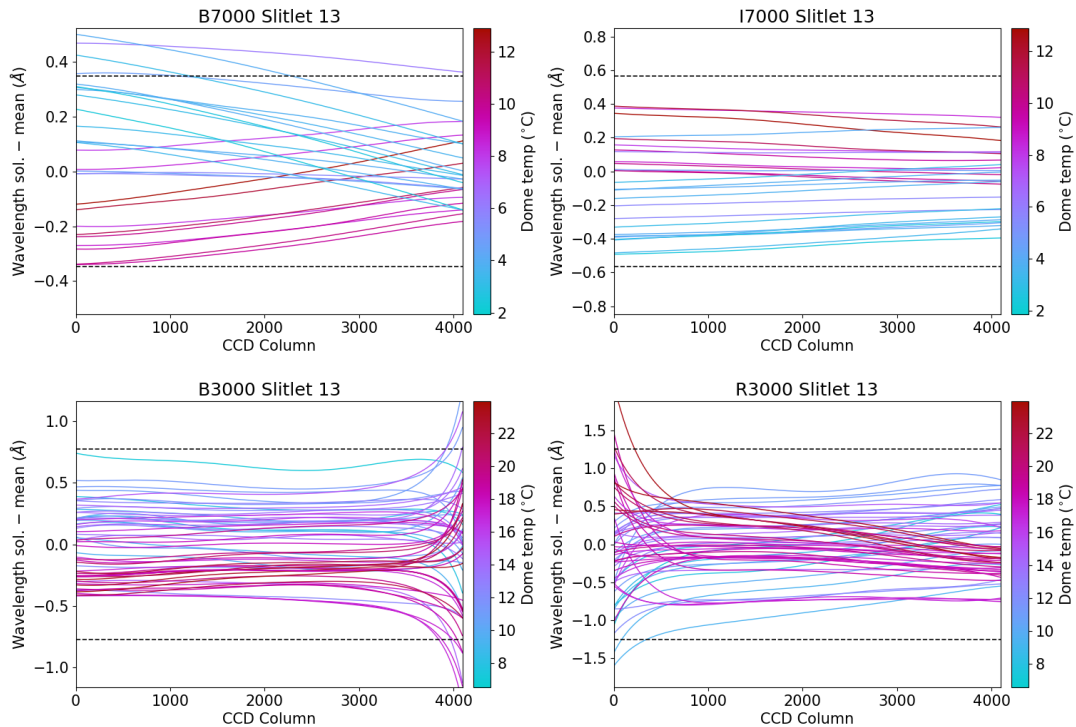


Figure 5. Difference in the wavelength solution over the CCD for each resolution and camera, compared to the mean for that resolution+camera combination. We show only the middle slitlet, but the others show similar overall trends (see Childress *et al.*, 2016). Each curve is a different arc lamp observation, coloured by the temperature recorded at that time. The dashed lines denote the size of a CCD pixel. $R = 7000$ shows similar levels of variation to $R = 3000$ (despite the differing wavelength dispersions), except at the CCD column boundary, where the variation is less extreme because a) throughput is higher at higher resolution (especially toward the ends of wavelength coverage where B3000 and R3000 drop to near 0; see Figure 1), and b) the wavelength solution for $R = 3000$ gratings is less stable in the dichroic region at high (low) CCD column numbers for B3000 (R3000).

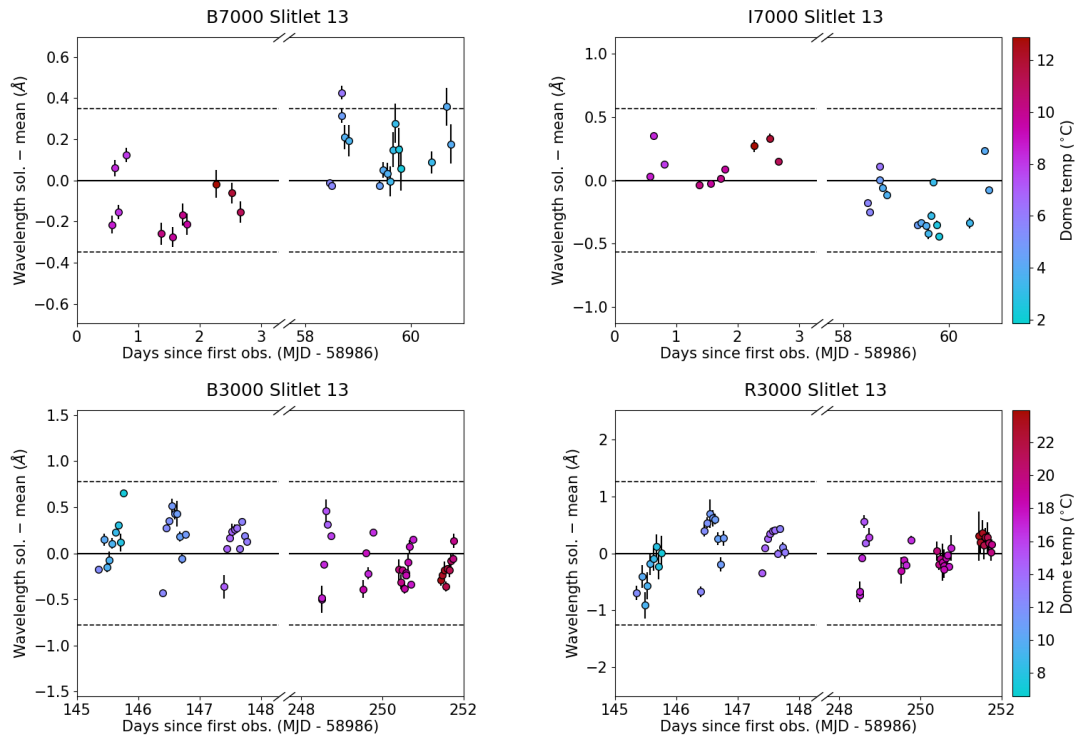


Figure 6. The same as Figure 5 but now averaged across the CCD column and as a function of observation date. The dependence on temperature is still clear, but now the seasonal dependence is seen by the grouping in different observation runs.

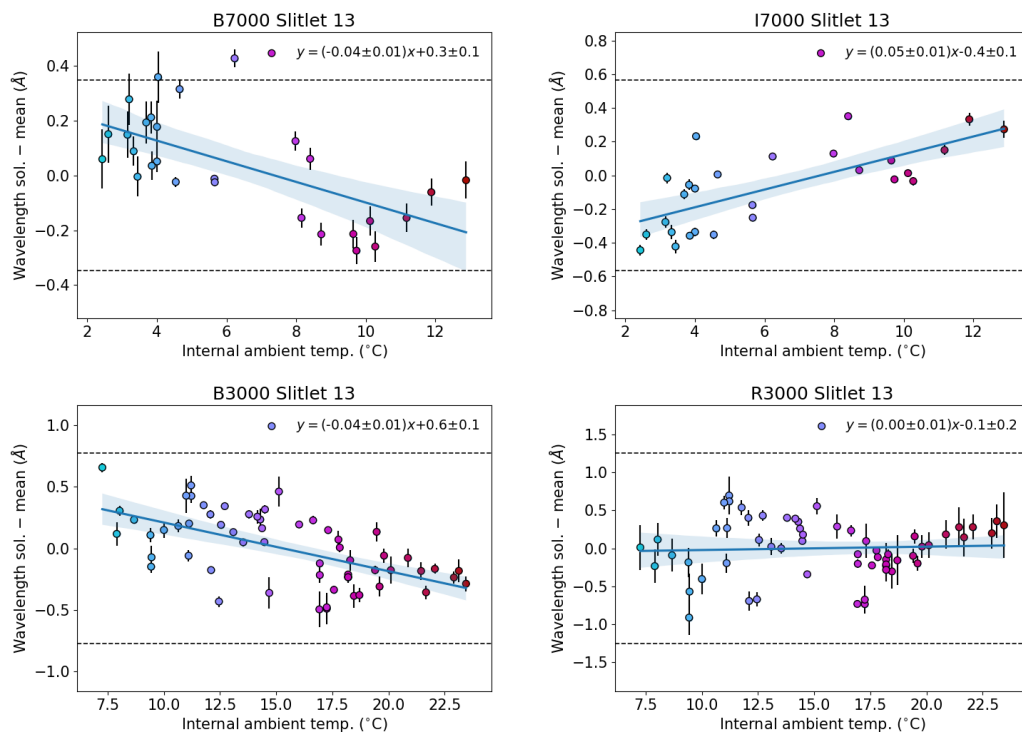


Figure 7. Average difference in wavelength solution as a function of temperature. The colour map is carried through from Figures 5 and 6, i.e. the x -axis here. Since we observed for a full year, our observations roughly capture the extremes of temperature during a typical year, so it is expected that the average wavelength solution will not vary by more than a CCD pixel. According to the linear relations fit to the temperature data, even if the temperature does vary more than expected, it would still be predominantly sub-pixel.

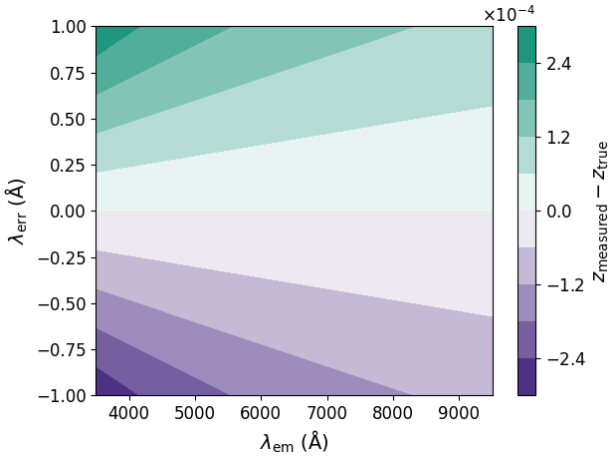


Figure 8. The redshift error resulting from measuring a spectral feature at λ_{em} up to $\pm 1 \text{ \AA}$ (λ_{err}) from its true value, due to, e.g. a small residual temperature dependence in the wavelength solution. We generally redshift features in the red ($\text{H}\alpha$, Ca triplet), and the average wavelength solution error is less than 0.5 \AA over most of the CCD (Figure 5), resulting in a realistic maximum redshift error of $\sim 6 \times 10^{-5}$. Sources whose features are primarily at low wavelengths could potentially experience larger errors.

always less than a CCD pixel (see Table 1), except for a couple of B7000 measurements. There are no long-term trends (albeit with only a single year of data) apart from the seasonal (temperature) difference. Even extreme temperature fluctuations are expected to cause an order $\sim 1 \text{ \AA}$ fluctuation in wavelength solution.

To put into perspective how a 1 \AA error would appear while redshifting, we show in Figure 8 the severity of measuring a spectral feature up to $\pm 1 \text{ \AA}$ off its true value for a source $z = 0.1$,^f over the full spectral range of WiFeS. The error is more severe at the blue end, but we generally use features in the red for redshifting. Over the entire CCD, the average temperature-induced shift is less than 0.5 \AA which we account for with frequent calibration, so the expected temperature-induced redshift error is much less than the maximum $\sim 0.5 \text{ \AA}$ or redshift of $\sim 6 \times 10^{-5}$ from Figure 8. Below, we show that when we redshift well-known objects/features, we indeed see a smaller average error.

4.2 Skylines

Skylines are strong emission lines, mostly in infrared, that come from our own atmosphere and need to be removed from our spectra. However, since they originate on Earth, we can use them as a test of wavelength solution in addition to arc lamps. For every science target, we ‘redshifted’ the sky spectrum (which is coincident with but separate from the science spectra due to the Nod&Shuffle mode of operation) in the centre and corners of the aperture to test how the wavelength solution varied across the field of view. For a small subset of the entire

^fWhile we set the source redshift to 0.1, there is no dependency on the redshift for this additive offset to the wavelength solution. We could equally consider a *stretch* to the wavelength solution, and this would act as an additional redshift.

science sample (one observation from every night), we did the same without any binning, i.e. we tested the wavelength solution of every spaxel since the S/N of the individual skylines is always very high. To get the redshift of a sky spectrum, we modified Marz to use a high S/N sky spectrum from the European Southern Observatory’s *skycorr* tool (Noll *et al.*, 2014) as a template. Figure 9 shows the average wavelength solution across the aperture, grouped by resolution. The $R = 3000$ gratings show more variation, but each only varies by $< 5 \times 10^{-5}$, and the central region is always accurate to within $\pm 2 \times 10^{-5}$.

Figure 10 shows the results of binning the central and outer regions separately for the high and low-resolution configurations. The $R = 7000$ gratings show little variability, especially in the centre. In every case, the mean offset is $< 2 \times 10^{-5}$, which corresponds to $< 0.1 \text{ \AA}$ in our observable sky-line spectral region (much less than any grating’s resolution).

4.3 Radial velocity standards

As a final test of the wavelength solution, we also observed radial velocity standard stars. The radial velocities of these stars are known precisely (Nidever *et al.*, 2002), so we can compare wavelength solution in a similar way to the known zero-redshift wavelength of skylines. Figure 11 shows the redshift difference of each observation of a radial velocity standard (some observations are of the same star on different nights), split by resolution mode. As expected, $R = 7000$ is much more precise, with an undetectable redshift bias, whereas $R = 3000$ has an offset of 5×10^{-5} . Both sets have < 10 observations so it is hard to conclude if there is any meaningful correction that needs to be made to the redshifts we obtain for other targets. Both sets are also skewed by a large outlier. When we investigated the outlier, we found that the arc lamp frame used to calibrate the spectrum notably influenced the redshift and that the observation ~ 0.5 hours after astronomical twilight differed in measured redshift by 7×10^{-5} from the observation ~ 2.5 hours after twilight. These two effects are seemingly unrelated, however, so this is an interesting example of how observing conditions may have unaccounted effects on redshifts.

All the radial velocity standards we chose were spectral type G or K, so we also tested how the stellar template used while redshifting affected the redshift, regardless of the actual spectral type. Thus we redshifted each star with both a G and a K-star template in Marz. Figure 12 shows the difference in redshift offset when each template was used. Note that we now make no distinction between resolution, and the G template histogram is exactly the combined distribution of Figure 11. Interestingly, the K-star template resulted in moderately biased redshifts, by $+7 \times 10^{-5}$, even if the star was itself K-type.

Naïvely, the best solution should be to redshift a star with the same spectral type template. However, one would also expect these two templates, in particular, would agree since the absorption features are similar for K and G. The difference between the two templates in Marz is that the G template covers a broader wavelength range than K and includes the calcium triplet. Assuming the broader wavelength coverage of the G-

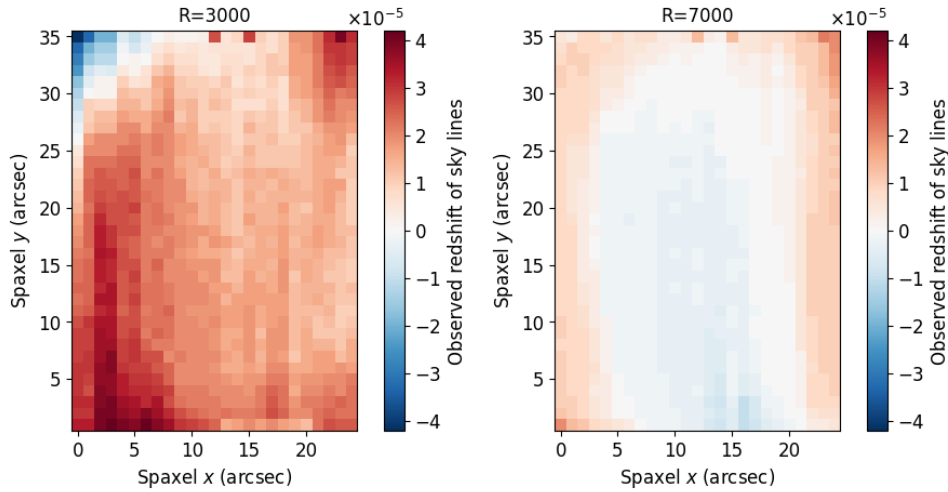


Figure 9. Wavelength solution (effectively redshift) calibration across the aperture per grating, found by means of ‘redshifting’ the $z = 0$ sky spectrum, with no spatial binning.

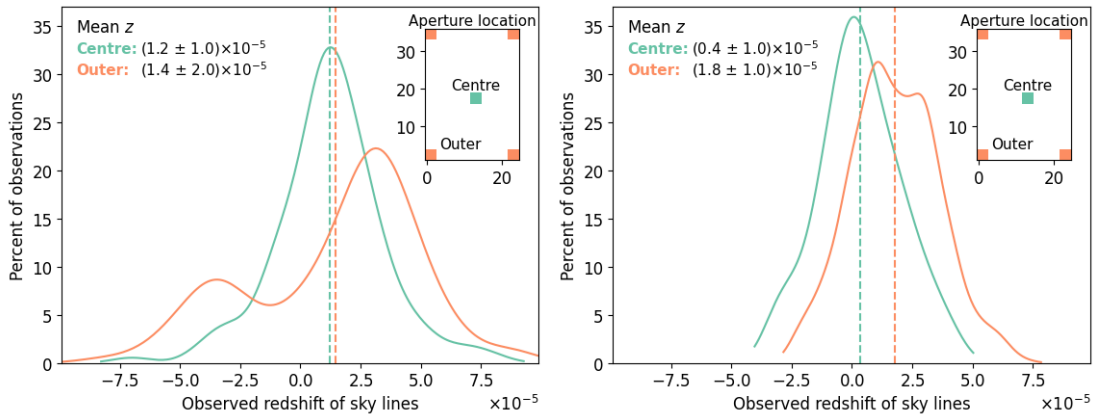


Figure 10. Wavelength solution/redshift calibration across the aperture with binning shown in the upper right of each panel, from redshifting the $z = 0$ sky spectrum. The left panel shows $R = 3000$ and the right panel shows $R = 7000$. These curves have been smoothed over the ~ 200 sky-spectrum observations for each individual aperture region. The double-peaked nature of the $R = 3000$ curve for the outer regions comes from the fact that the upper left corner is generally bluishifted, and the upper right and lower left redshifted from the centre (see Figure 9). This is also the case for $R = 7000$ but to a much lesser extent.

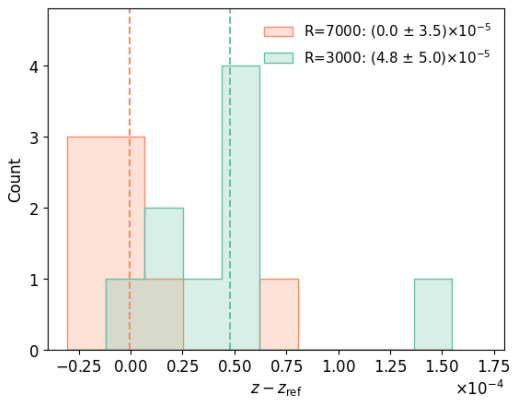


Figure 11. Redshift offset from our observations compared to the published radial velocities of radial velocity standards. Again the higher resolution performs better, but both suffer from a large positive outlier.

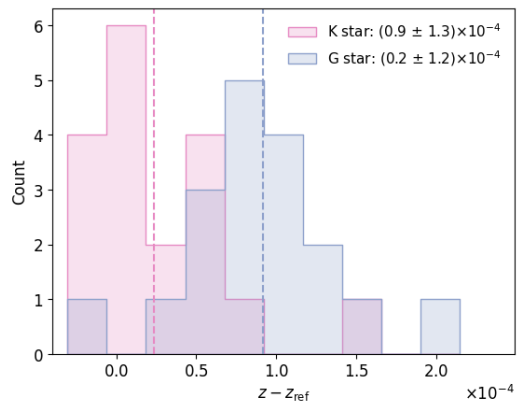


Figure 12. Redshift offset of all radial velocity standards regardless of resolution, but redshifted using different stellar templates in Marz. There is a disparity between the average redshift as measured by each template spectral type.

type stellar template is the main reason for the disagreement, we opted to redshift all the radial velocity standards with this template. In addition, our redshifts from the G-star template show better agreement with the published radial velocities in every case.

Apart from this moderate disagreement between stellar templates, none of our investigations into the accuracy of our wavelength solution revealed any need to further calibrate our redshifts. The stellar template problem is interesting and may require further investigation, although in the case of galaxies it remains important to redshift with the template that best matches. A high S/N galaxy spectrum can be redshifted by an early, intermediate or late-type template, but the redshift may shift up to a couple of 10^{-4} depending on which main features the target and template galaxy displays. As such, we always redshift galaxies with their matching template in Marz.

From our investigations, we are assured our redshifts are accurate to within several 10^{-5} .

5. Results

5.1 Redshift performance and comparison

Most galaxies (161/185) are bright and large enough in the sky to obtain at least one redshift at different spatial locations with which we can characterise the average redshift. Others (24/185), however, were too small, dim, or otherwise had too little S/N to obtain multiple redshifts, so instead the entire galaxy was redshifted. The average redshift also reflects the systemic redshift of the galaxy provided that the aperture was centred on the galaxy. Since this is not always the case, we also redshift just the core section of the galaxy, where possible, to compare to. This comparison is shown in Figure 13. The mean offset is -8.4×10^{-6} , and the scatter is of the order of several 10^{-5} . The agreement on average is as good as we can expect given our investigations into the accuracy of the wavelength solution, but the scatter is also affected by the S/N, whether

the galaxy was centred in the aperture, and whether the galaxy was early or late-type. The largest outlier is the host of SN 2009Y, NGC 5728, which has very strongly double-peaked emission lines, even in the central region. In this case, the Ca triplet is much preferred to redshift from but was not always present with high S/N.

We present the results of our redshifting in Table A1 and Figure 13. We find a mean systematic offset of 4.3×10^{-5} with normalised median absolute deviation (NMAD) of 1.2×10^{-4} between our redshifts and Pantheon+, which, as shown by Carr *et al.* (2022) is negligible for SN cosmology. However, surprisingly, there are several redshift discrepancies above the level of 10^{-3} , and we show the two largest in Figure 14. The features in red are shown at the old redshift, while the template we used to redshift is shown at our measured redshift. The Pantheon+ redshift of the host of SN 2006kf comes from a single-peaked 21-cm Hydrogen emission feature (Springob *et al.*, 2005), while SN 2016hpx was redshifted as part of the Foundation Supernova Survey from the publicly available SN classification spectrum that showed possible weak host galaxy H α emission (Foley *et al.*, 2018; Dimitriadis *et al.*, 2016). Neither of these historical redshift examples came from optical host galaxy spectra.

For SN 2006kf, the redshift originally came from single-peaked 21 cm profile according to the NASA/IPAC Extragalactic Database.^g A low S/N double horn distribution could potentially be mistaken for a single horn, and therefore could bias the redshift determination by the rotation of the galaxy.

For SN 2016hpx, of the two publicly available spectra (different reductions of the same spectrum) on the Weizmann Interactive Supernova Data Repository^h (WiSeREP), one does indeed show a faint peak in the wavelength region that would be consistent with a host galaxy around $z = 0.033$; however,

^gSeen in the comment of the NED record, from Springob *et al.* (2005).

^h<https://www.wiserep.org/object/9647>

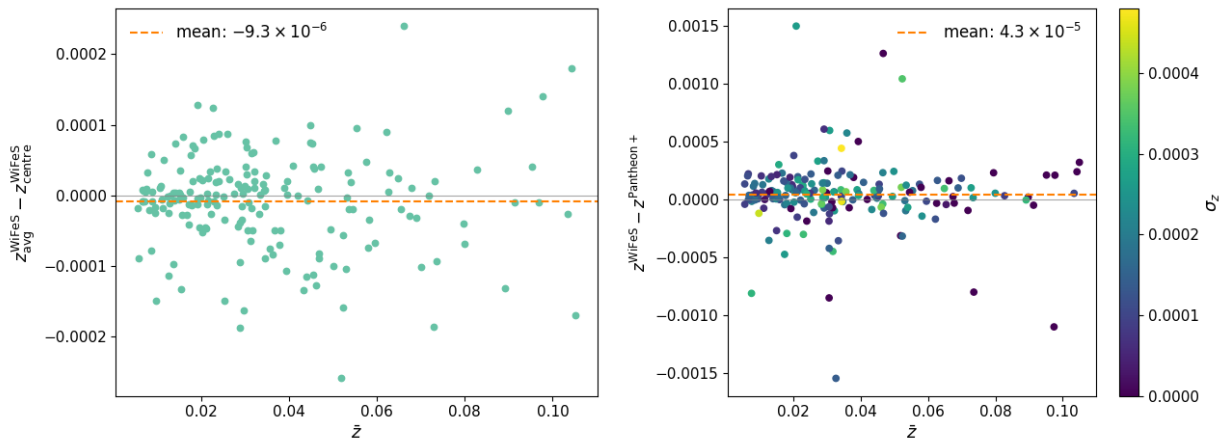


Figure 13. **Left:** Self-consistency between the average redshift over all Voronoi spaxel bins in each galaxy and just the core section. **Right:** Difference in the redshift of each galaxy as averaged over all spaxel bins from WiFeS (this work) and Pantheon+, coloured by the standard deviation in redshift over each spaxel bin within each galaxy. The mean offset is 4.3×10^{-5} , and insensitive to the outliers, which are interesting in themselves. The mean offset is similar in both panels, but the scatter in the self-consistency check in the left panel is nearly an order of magnitude smaller than the comparison with Pantheon+ redshifts in the right panel.

the other does not. This could be a chance detection of a faint emission line, but it is only a single, weak feature and the spectra are low resolution and quality. The discrepancy with our measurement would be consistent with the original redshift being mistaken as it is not a case of galactic rotation since the host, LEDA 762493, is almost face-on and the SN occurred only $3''$ from the core.

Intriguingly, the magnitude of the offset with Pantheon+ is almost exactly that of the average geocentric correction of 11.7 km s^{-1} ($z = 3.9 \times 10^{-5}$) we apply to our redshifts. Since the offset is so small, the most likely reason we see it is just due to chance. Perhaps it could imply that the historical redshifts from Pantheon+ did not have a geocentric correction applied, but this is difficult to test, as it requires the exact observation location and time. In any case, the individual large redshift discrepancies are potentially more interesting than this small systematic offset.

5.2 Redshift uncertainty

Since in most cases we have many spectra for the same galaxy and many features in those spectra, we can estimate the variation in redshift caused by noise as a measure of precision. We can do this in two ways: the first is to measure the variation of wavelength determination of individual features, and the second is to measure the variation between multiple features. Both can be achieved by redshifting many realisations of each spectrum with the flux of each pixel shifted by a Gaussian whose standard deviation is the measured noise of that pixel. The method that utilises multiple features is more appropriate for characterising redshift uncertainty as redshifting from a single feature is very rarely trustworthy (unless it is particularly high S/N and/or has resolved substructure), but here we already have a tight prior on the redshift, and we are mainly interested in its variation rather than its value. Instead of running each realisation of each spectrum through Marz, we opt to fit the features using Gaussians and convert the central wavelength to a redshift. This method is highly scaleable (no user interface and low computation time); however, it may still be interesting to compare the robust correlation method to the simplified Gaussian fitting. Note that we cannot simply use the width of the correlation peak given by Marz to estimate redshift uncertainty as it is at least an order of magnitude larger than our actual precision.

Each spectrum was assigned tags for which features were present with enough S/N to be able to at least somewhat reliably fit Gaussians (both absorption and emission). 500 realisations of each spectrum were generated, and a $\pm 30 \text{ \AA}$ rest wavelength window containing each feature was extracted, using the outer edges to estimate and subtract the continuum. A Gaussian was then fit to each feature; the fit was rejected if it was more than 10 \AA from the known wavelength, if it was unreasonably wide or low amplitude, (accounting for the fact absorption lines are generally wider and shallower than emission), and if the amplitude was positive (negative) for emission (absorption) lines, all of which indicate a failure to capture the feature of interest. A five \AA rest wavelength window around

the known wavelength was also used to estimate the S/N of each feature from the original spectrum.

The features we applied this process to were: $H\alpha$, $H\beta$ (both of which can be in both emission and absorption), $H\gamma$, Na, Mg, the second line of each of O[II], O[III], N[II], S[II], H+K absorption, and the Calcium triplet. The NMAD of the fitted wavelengths measures how much the redshift can shift within the bounds of the measured noise, and when plotted against S/N shows a strong trend of increasing precision with increasing S/N. The mean of all of the fitted wavelengths when compared with the known redshift measures how much the redshift can shift according to which features are present or most prominent. This in particular should be a more accurate reflection of the total redshift precision. Given the type of galaxy/features and S/N, an estimate of redshift precision can be made. Ideally this would be done on an individual redshift basis, but we save a more thorough treatment for future work.

Figure 15 shows examples of the methods described above and Table 2 shows the numerical results. Figure 15a shows the ‘intra-line’ variation of the $H\alpha$ emission and Na absorption features against their S/N estimates, while Figure 15b shows an example of the average Gaussian fit to the 500 realisations of the Calcium triplet of one spaxel bin of NGC 2962 (host of SN 1995D). The S/N is just an estimate because the five \AA window used to estimate it is too wide for some emission lines and too narrow for some absorption lines. Occasionally, the noise is overestimated and/or the flux is underestimated (e.g. the cases of reduction failures), which is why we see $S/N < 1$ but solid feature detection. Finally, emission lines are naturally higher S/N than absorption lines, so 1:1 comparisons between the two can be misleading. In general though, especially at high S/N, which was the aim of this program, we see excellent precision. However, some features do not show a trend with S/N (such as the hydrogen absorption lines and Calcium H+K), which may be due to their presence at lower S/N in general and/or a Gaussian fit being less appropriate.

Figure 15c shows the offset from redshifting a single feature compared to the Marz redshift. These measurements are found from taking the mean of the mean offsets for each feature and spaxel bin compared to their Marz measured redshift. The emission lines are generally in much closer agreement with the final redshift measurement; the reason Mg and Na in particular are not in agreement is due to their complex line-profiles. Since these lines are (sometimes significantly) asymmetrical and deeper in the blue end than the red, the fitted wavelength is biased blue. While the Gaussian fit for these lines is biased, the intra-line variation should be robust to the exact location of the centre of the Gaussian approximation.

In conclusion of this investigation, the high S/N emission line galaxy redshifts are precise to better than several 10^{-5} , the high S/N absorption galaxies and low S/N emission line galaxies are precise to better than approximately 1×10^{-4} , and the low S/N absorption galaxies are not generally present.

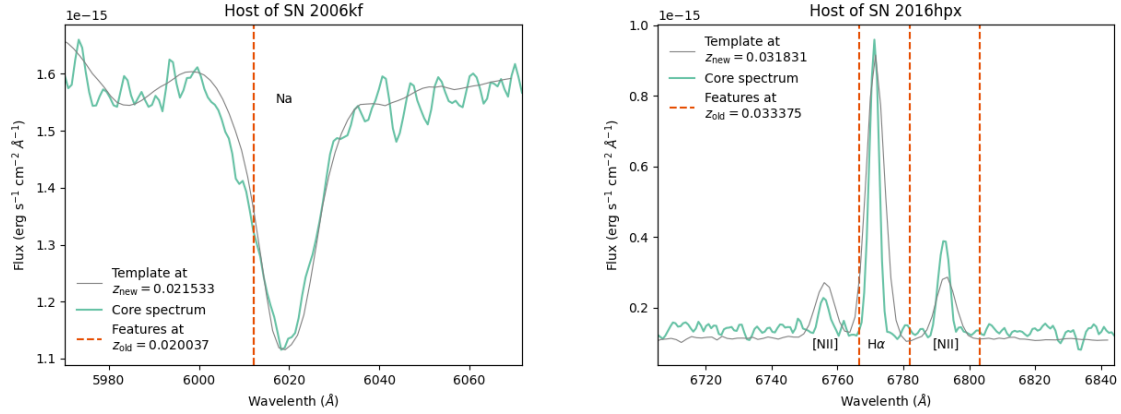
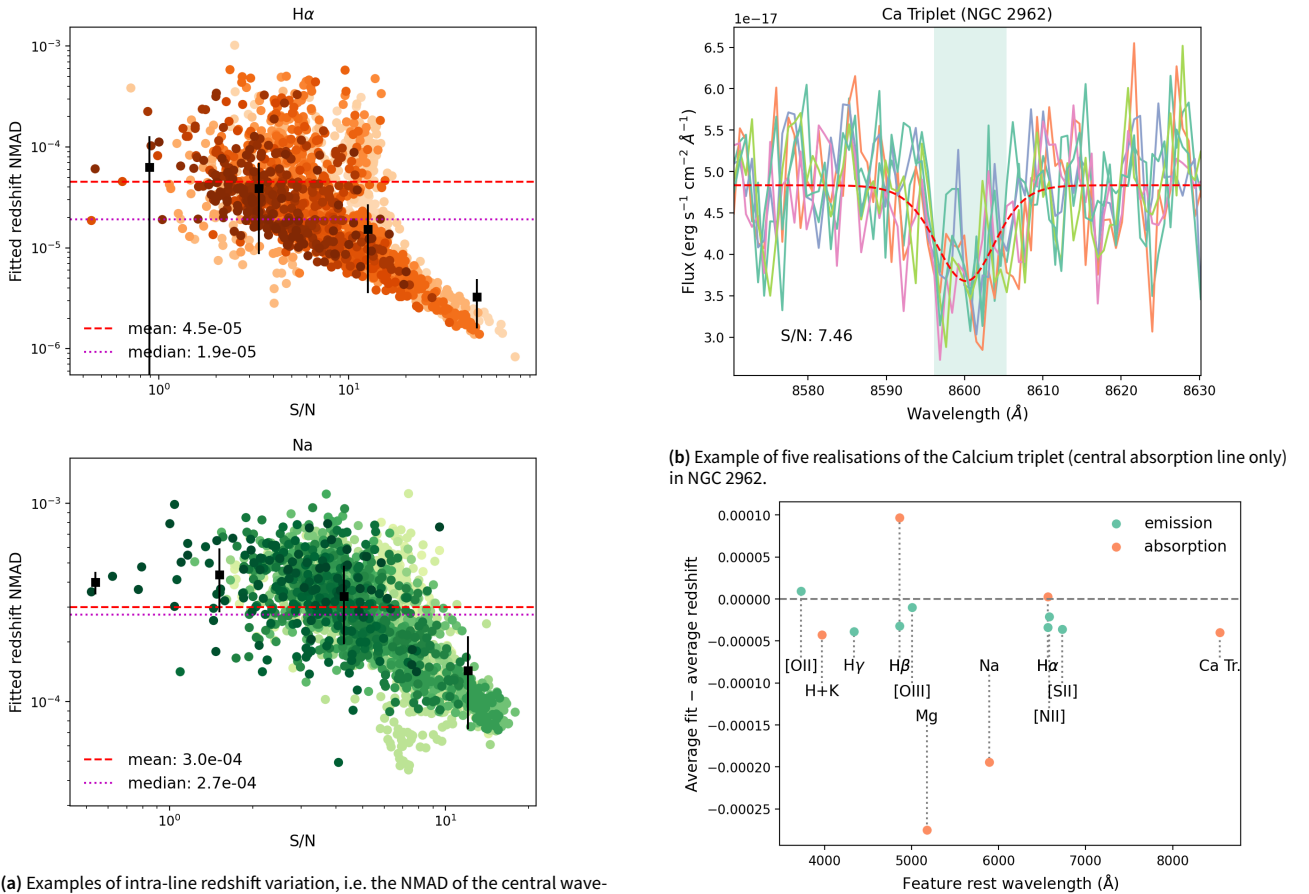
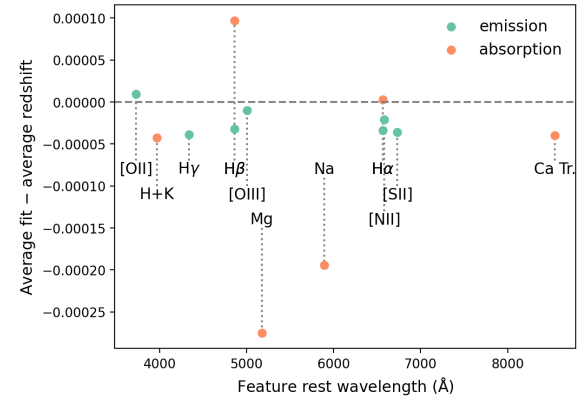


Figure 14. Comparison of WiFeS redshifts (new) to Pantheon+ redshifts (old) in the cases of the two largest discrepancies. Our redshifts are shown by our measured spectra (green), obtained at very high S/N from the core section of each galaxy, and by the grey templates, while the relevant feature locations at the Pantheon+ redshift are shown with red dashed lines.



(a) Examples of intra-line redshift variation, i.e. the NMAD of the central wavelength of Gaussians fit to 500 Monte-Carlo realisations of each feature of each spectrum. The top panel shows each spaxel bin displaying H α emission and the bottom shows Na absorption.

(b) Example of five realisations of the Calcium triplet (central absorption line only) in NGC 2962.



(c) Variation in redshift between the mean of each feature measured individually and the corresponding spaxel bin redshift measured in the main analysis.

Figure 15. **a)** shows the variation in fits to the central wavelength of the individual features of H α emission and Na absorption. Each spectrum was realised 500 times, varying the pixel flux by a Gaussian with a width of the measured noise, then Gaussians were fit to those features. Each point in these figures is the variation in those centres, converted to redshift, and each galaxy is a different colour. The mean and median of these are shown in the red dashed and magenta dotted lines respectively, and overplotted in black are the binned data. **b)** shows five of the 500 realisations in solid lines of a particular spaxel bin of the galaxy NGC 2962. The red dashed line shows the normalised sum of all 500 fitted Gaussians. The green window is a five \AA rest wavelength window about the canonical redshift used to estimate the S/N of the feature. **c)** shows the variation caused by measuring single features when compared to the redshift measured from Marz, with emission (green) and absorption (orange) differentiated (H α and H β occur in both, sometimes within different regions of the same galaxy). The dotted lines are simply to aid in identifying each feature.

Table 2. Summary of spectral feature fitting precision, converted to redshift. Rest wavelengths are taken from Marz and converted from vacuum to air, except for the Calcium triplet which comes from the Vienna Atomic Line Database.

Feature	Rest wavel. (Å)	Mean NMAD	Med. NMAD	Diff. from z_{hel}
O[II]	3727.425	4.2×10^{-4}	4.2×10^{-4}	9.5×10^{-6}
H+K	3968.468	6.0×10^{-4}	5.9×10^{-4}	-4.3×10^{-5}
H γ	4340.469	2.0×10^{-4}	1.5×10^{-4}	-3.9×10^{-5}
H β (em.)	4861.325	1.2×10^{-4}	7.4×10^{-5}	-3.2×10^{-5}
H β (abs.)	4861.325	5.3×10^{-4}	5.0×10^{-4}	9.7×10^{-5}
O[III]	5006.843	1.5×10^{-4}	1.1×10^{-4}	-1.0×10^{-5}
Mg	5175.3	5.6×10^{-4}	5.6×10^{-4}	-2.8×10^{-4}
Na	5894.0	3.0×10^{-4}	2.7×10^{-4}	-1.9×10^{-4}
H α (em.)	6562.80	4.5×10^{-5}	1.9×10^{-5}	-3.4×10^{-5}
H α (abs.)	6562.80	3.3×10^{-4}	3.0×10^{-4}	2.9×10^{-6}
N[II]	6583.408	7.9×10^{-5}	5.2×10^{-5}	-2.1×10^{-5}
S[II]	6730.849	1.5×10^{-4}	1.2×10^{-4}	-3.6×10^{-5}
Ca triplet	8542.088	2.0×10^{-4}	1.8×10^{-4}	-4.0×10^{-5}

5.3 Cosmological Results

To quantify the effect of our redshift updates on cosmology, we use the entire SH0ES/Pantheon+ cosmology sampleⁱ (photometry and Cepheid calibration) and the PIPPIN^j end-to-end SN cosmology analysis pipeline (Hinton & Brout, 2020). This method allows us to calculate SH0ES/Pantheon+ distance moduli using the redshifts of this work as well as take advantage of the statistical+systematic covariance matrix C for both the original and updated redshift sample. For each of the redshifts we remeasure, we transform to the CMB frame then recalculate peculiar velocity using `pvhub`^k to correct to the cosmological frame (z_{HD}). The average change in peculiar velocity was zero, but individually they varied by up to $\pm 80 \text{ km s}^{-1} \text{ Mpc}^{-1}$.^l

With our new set of cosmological redshifts z_{HD} , Pantheon+ light-curves and SH0ES calibrations, we perform a simultaneous fit for H_0 and Ω_m in a flat Λ CDM Universe (i.e. $\Omega_\Lambda = 1 - \Omega_m$, $w = -1$) by minimising distance modulus residuals defined by

$$\Delta\mu_i = \mu_{\text{obs},i} - \mu_{\text{model}}(z_{\text{HD},i}, H_0, \Omega_m), \quad (1)$$

where i spans the set of Pantheon+ light-curves. Briefly, PIPPIN makes use of SNANA (Kessler et al., 2009) to take input photometry, redshifts, etc. and calculate $\mu_{\text{obs},i}$ from a modified Tripp equation of the form

$$\mu_{\text{obs}} = m + \alpha x_1 - \beta c - M - \delta_{\text{bias}} + \delta_{\text{host}}, \quad (2)$$

where light-curve peak magnitude m (equivalent to B -band magnitude), stretch x_1 and colour c are fit with an updated SALT2 model (Guy et al., 2010; Brout et al., 2022b), α and β are nuisance parameters, M is the absolute magnitude of SNe

ⁱ<https://github.com/PantheonPlusSH0ES/DataRelease>

^j<https://github.com/dessn/Pippin>

^k<https://github.com/KSaid-1/pvhub>

^lThe peculiar velocity field used in `pvhub` is a discretised grid in redshift-space, and smoothed with a Gaussian kernel of width $4 h^{-1} \text{ Mpc}$. The peculiar velocities only change for the galaxies that are close enough to cell walls that a small redshift change causes them to fall into a new cell.

Ia, δ_{bias} are observational bias corrections estimated from simulations, and δ_{host} accounts for the residual correlation between SN Ia brightness and host mass. For more details, see Hinton & Brout (2020); Brout et al. (2022a). The theoretical distance moduli μ_{model} are calculated directly from the cosmological model as

$$\mu_{\text{model}}(z) = 5 \log_{10}(D_L(z)) + 25, \quad (3)$$

with luminosity distance D_L in Mpc, calculated from

$$D_L(z) = (1+z) \frac{c}{H_0} \int_0^z \frac{dz'}{\sqrt{\Omega_m(1+z')^3 + 1 - \Omega_m}}. \quad (4)$$

For Cepheid calibrated galaxies, $\mu_{\text{model}}(z_i)$ is replaced with μ_i^{Cepheid} . With the vector of residuals $\Delta\mu$, the best-fit cosmology comes from minimising the function

$$\chi^2 = \Delta\mu^T C^{-1} \Delta\mu. \quad (5)$$

Of the 185 SN host galaxies we measured, 146 galaxies and 215 light-curves passed the quality cuts to be used in the fit.

This determination of H_0 is equivalent to fitting the intercept of the linear distance-redshift relation, as done by SH0ES (Riess et al., 2022). The intercept, a_B , is constrained by galaxies whose motion is dominated by expansion. It is standard practice to use the (third-order) cosmographic expansion of recession velocity, which is almost exact in the ‘Hubble Flow’ redshift range used for fitting H_0 ($0.0233 < z_{\text{HD}} < 0.15$):

$$\begin{aligned} \log_{10} H_0 &\approx \log_{10} \left[\frac{cz}{6} \left(6 + 3(1-q_0)z + (1-q_0 - 3q_0^2 + j_0)z^2 \right) \right] \\ &\quad + \frac{1}{5} (-m_B + M_B + 25) \\ &\equiv a_B + 0.2M_B + 5. \end{aligned} \quad (6)$$

The expansion includes the cosmic deceleration parameter ($q_0 = -0.55$) and jerk ($j_0 = 1.0$), whose values are chosen to match the standard Λ CDM model with $(\Omega_m, \Omega_\Lambda, w) = (0.3, 0.7, -1)$. As such, this fitting method has weak cosmological model dependence. Since the dependence is weak, this method can still be used to constrain cosmologies whose parameters are somewhat near the input parameters.

An input cosmology also enters into our analysis in the simulations used to perform bias corrections, and this dependence is also weak (Camilleri et al. in prep.). The results of our fit are shown in Figure 16; the Hubble diagram of the updated sample has a best-fit cosmology $(H_0, \Omega_m) = (72.6 \pm 1.2 \text{ km s}^{-1} \text{ Mpc}^{-1}, 0.328_{-0.017}^{+0.018})$, and the weighted average difference in distance moduli is only $-5 \times 10^{-4} \text{ mag}$. The error bars we show are the statistical and systematic uncertainties from the covariance matrix, added in quadrature. It should be noted that even when including the 250 km s^{-1} uncertainty in peculiar velocities ($\sim 8 \times 10^{-4}$ when converted to redshift), redshift uncertainties propagated through to H_0 are completely subdominant to these distance modulus uncertainties.

Since we are using magnitudes calibrated with SH0ES, we see a similar central values of H_0 to SH0ES ($73.04 \text{ km s}^{-1} \text{ Mpc}^{-1}$; Riess et al., 2022), but only the shift in H_0 from our redshift

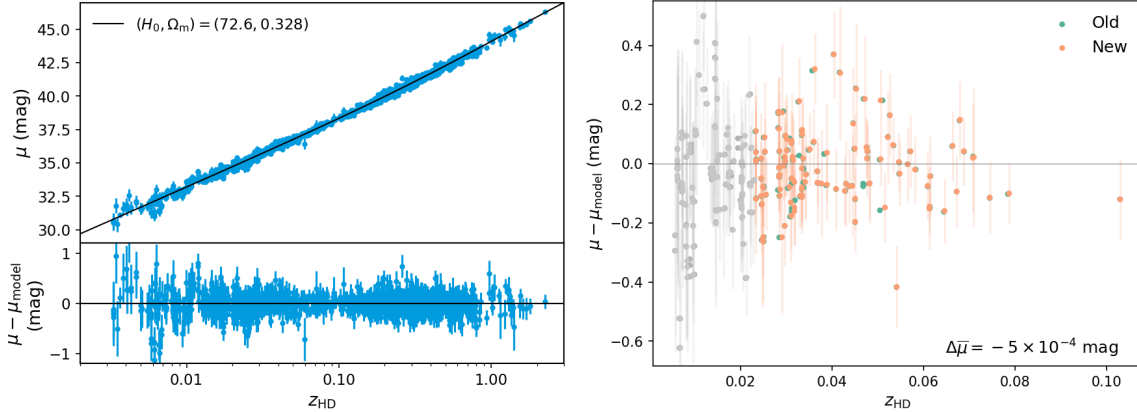


Figure 16. **Left:** full Hubble diagram showing the SNe used to constrain and the residuals of the best-fit flat Λ CDM cosmology $(H_0, \Omega_m) = (72.6 \text{ km s}^{-1} \text{ Mpc}^{-1}, 0.328)$. **Right:** change in individual μ , normalised to the best-fit cosmology of the updated redshift sample. Galaxies with $z_{\text{HD}} < 0.0233$ are greyed out because they are not used to determine H_0 . The change from original (green) to updated (orange) in magnitude space is often too small to see. The error bars, shown only for the updated sample, come from the covariance matrix statistical and systematic uncertainty added in quadrature (for display purposes only). The weighted average shift in μ of -5×10^{-4} mag from the original sample corresponds to a shift in H_0 of $+0.1 \text{ km s}^{-1} \text{ Mpc}^{-1}$.

changes is important here. Thus, the key takeaway from this work is that the shift in H_0 from the original sample purely due to our redshift updates is only $0.1 \text{ km s}^{-1} \text{ Mpc}^{-1}$, which is negligible compared to the $1.2 \text{ km s}^{-1} \text{ Mpc}^{-1}$ uncertainty of each fit. We can also calculate an individual H_0 directly for each of the host galaxies in our sample from Equation (4) with $\Omega_m = 0.3$, replacing the left-hand-side with $D_L(\mu_{\text{obs}})$, and taking the weighted average before and after the redshift updates gives the same result of $0.1 \text{ km s}^{-1} \text{ Mpc}^{-1}$. This is not unexpected from the magnitude of the changes to redshift, and a similar result was found in Carr *et al.* (2022) although opposite in sign. The average redshift correction was an order of magnitude larger in Carr *et al.* (2022) in the same direction, so the result of this work is likely just a statistical fluctuation. Our result reinforces the general conclusion that while redshift errors have the potential to bias H_0 , the reality is that any realistic redshift errors are too small to affect H_0 .

6. Conclusion

We have shown with our new observations that indeed there exist errors in the previous measurements of the redshifts of nearby SN Ia host galaxies. The differences had a negligible systematic offset, which was reflected in the negligible change to H_0 .

We have shown our redshifts to be accurate to within a couple of 10^{-5} . However, there are several extensions to our analysis that can be made to further investigate the sources of the redshift errors in the interest of mitigating redshift errors in the future. Firstly, while we saw good agreement between averaging the redshift over all spaxels and just the core sections, it would be beneficial to investigate why we still see scatter at the level of about 3×10^{-5} . In addition, the rest of the cases of very large redshift discrepancies (rather than just the two largest) can be examined by comparing with original spectra where possible. Finally, for many galaxies (about half of our sample), we will be able to redshift the region around where

the SN actually occurred within the galaxy. This would be a useful crosscheck with previous redshifts, as there may be a correlation between those redshifts and the historical redshifts of Pantheon+ in the cases where a slit spectrograph was aligned with the SN but not the core, or a fibre pointing inaccuracy. It is also useful for observing the local SN environment and examining SN Ia brightness and host/environment correlations, as there is a wealth of information beyond the redshifts to explore.

In this work, we study the overall accuracy and precision of our redshifts, but we have not characterised individual precisions for our redshifts, which would be a function of the spectrum S/N and number of spaxel bins for a galaxy. Instead we give a general uncertainty class depending on the S/N and galaxy type/prominent features. This can be taken further to provide individual estimates, which would mostly be useful to differentiate the lower quality observations, as our high S/N data are extremely accurate and precise for an optical spectrograph without simultaneous wavelength solution measurement (from, e.g., frequency combs). For the purposes of measuring H_0 , our redshift data can essentially be taken as constants, at least until the peculiar velocity and distance modulus uncertainty floor is drastically improved. This has already been done historically for convenience, but for our sample this is a valid assumption; however, it does not necessarily hold for other purposes which may be even more sensitive to redshift errors.

While we have confirmed that remeasuring accurate redshifts does not have an effect on H_0 , we stress it is still important to use accurate and precise redshifts for cosmology, especially as we gather more and more spectroscopic data. Importantly, at least at high-redshift, we will have to start using photometric redshifts and SN classifications, as spectroscopic follow-up becomes unfeasible from the expected volume of data from future surveys, such as the Legacy Survey of Space and Time, which will add new forms of systematic error to investigate.

Data Availability

The spectroscopic data obtained as part of this work are available from the corresponding author upon reasonable request.

Acknowledgement

The authors thank S. Sweet for useful discussions and advice on observation optimisation. The authors thank C. Howlett, J. Calcino and K. Said for assistance in carrying out observations and M. Craigie for assistance in target selection.

TMD is the recipient of an Australian Research Council Australian Laureate Fellowship (project number FL180100168) funded by the Australian Government. DS is supported by DOE grant DE-SC0010007, DE-SC0021962 and the David and Lucile Packard Foundation. DS is supported in part by the National Aeronautics and Space Administration (NASA) under Contract No. NNG17PX03C issued through the Roman Science Investigation Teams Programme.

This work is based on data acquired at Siding Spring Observatory with the ANU 2.3m Telescope via programs 1200040, 2200080, 3200100 and 4200059. We acknowledge the traditional custodians of the land on which the telescope stands, the Gamilaraay people, and pay our respects to elders past and present. This research was also supported by resources provided by the University of Chicago Research Computing Center and used services provided by the Astro Data Lab at the US National Science Foundation's National Optical-Infrared Astronomy Research Laboratory. NOIRLab is operated by the Association of Universities for Research in Astronomy (AURA), Inc. under a cooperative agreement with the National Science Foundation. This work has also made use of the VALD database, operated at Uppsala University, the Institute of Astronomy RAS in Moscow, and the University of Vienna.

References

- Brout, D., Scolnic, D., Popovic, B., et al. 2022a, *ApJ*, 938, 110
 Brout, D., Taylor, G., Scolnic, D., et al. 2022b, *ApJ*, 938, 111
 Cappellari, M., & Copin, Y. 2003, *MNRAS*, 342, 345
 Carr, A., Davis, T. M., Scolnic, D., et al. 2022, *PASA*, 39, e046
 Childress, M. J., Vogt, F. P. A., Nielsen, J., & Sharp, R. G. 2014, *Ap&SS*, 349, 617
 Childress, M. J., Tucker, B. E., Yuan, F., et al. 2016, *PASA*, 33, e055
 Davis, T. M., Hinton, S. R., Howlett, C., & Calcino, J. 2019, *MNRAS*, 490, 2948
 Dimitriadis, G., Pursiainen, M., Smith, M., et al. 2016, *The Astronomer's Telegram*, 9704, 1
 Dopita, M., Hart, J., McGregor, P., et al. 2007, *Ap&SS*, 310, 255
 Dopita, M., Rhee, J., Farage, C., et al. 2010, *Ap&SS*, 327, 245
 Foley, R. J., Scolnic, D., Rest, A., et al. 2018, *MNRAS*, 475, 193
 Guy, J., Sullivan, M., Conley, A., et al. 2010, *A&A*, 523, A7
 Hinton, S., & Brout, D. 2020, *The Journal of Open Source Software*, 5, 2122
 Kessler, R., Bernstein, J. P., Cinabro, D., et al. 2009, *PASP*, 121, 1028
 Nidever, D. L., Marcy, G. W., Butler, R. P., Fischer, D. A., & Vogt, S. S. 2002, *ApJS*, 141, 503
 Noll, S., Kausch, W., Kimeswenger, S., et al. 2014, *A&A*, 567, A25
 Peterson, E. R., Kenworthy, W. D., Scolnic, D., et al. 2022, *ApJ*, 938, 112
 Planck Collaboration, Aghanim, N., Akrami, Y., et al. 2020, *A&A*, 641, A1
 Popovic, B., Brout, D., Kessler, R., Scolnic, D., & Lu, L. 2021, *ApJ*, 913, 49
 Riess, A. G., Yuan, W., Macri, L. M., et al. 2022, *ApJ*, 934, L7

- Sako, M., Bassett, B., Becker, A. C., et al. 2018, *PASP*, 130, 064002
 Scolnic, D. M., Jones, D. O., Rest, A., et al. 2018, *ApJ*, 859, 101
 Springob, C. M., Haynes, M. P., Giovanelli, R., & Kent, B. R. 2005, *ApJS*, 160, 149
 Yuan, W., Macri, L. M., Riess, A. G., et al. 2022, *ApJ*, 940, 64

Appendix 1. Supplementary Data Tables

Table A1. Redshift results. For each Type Ia SN we targeted, its Pantheon (source catalogue) ID is listed along with its host galaxy ID if it has one. Also listed is the redshift from the main analysis ($z_{\text{hel}}^{\text{WiFeS}}$) and the number of spaxels it was measured from (N_z), along with the redshift from the central region only ($z_{\text{hel,centre}}^{\text{WiFeS}}$). The corresponding redshift from Pantheon+ ($z_{\text{hel}}^{\text{Pantheon+}}$) is shown along with its difference from $z_{\text{hel}}^{\text{WiFeS}}$.

SN	Host	$z_{\text{hel}}^{\text{WiFeS}}$	N_z	$z_{\text{hel,centre}}^{\text{WiFeS}}$	$z_{\text{hel}}^{\text{Pantheon+}}$	$z_{\text{hel}}^{\text{WiFeS}} - z_{\text{hel}}^{\text{Pantheon+}}$
1993ae	IC 0126	0.019 776	15	0.019 780	0.019 667	1.1×10^{-4}
1994M	NGC 4493	0.023 161	23	0.023 160	0.023 083	7.8×10^{-5}
1995ak	IC 1844	0.022 815	71	0.022 730	0.022 699	1.2×10^{-4}
1995D	NGC 2962	0.006 558	23	0.006 550	0.006 561	-3.2×10^{-6}
1996Z	NGC 2935	0.007 548	72	0.007 540	0.007 565	-1.7×10^{-5}
1998es	NGC 0632	0.010 633	23	0.010 620	0.010 571	6.2×10^{-5}
1999ef	UGC 00607	0.038 941	16	0.038 930	0.038 857	8.4×10^{-5}
1999gh	NGC 2986	0.007 743	37	0.007 710	0.007 705	3.8×10^{-5}
2001da	NGC 7780	0.017 335	15	0.017 330	0.017 381	-4.6×10^{-5}
2001ic	NGC 7503	0.044 123	21	0.044 130	0.044 089	3.4×10^{-5}
2002ck	UGC 10030	0.029 827	29	0.029 815	0.029 742	5.8×10^{-5}
2002cr	NGC 5468	0.009 452	32	0.009 470	0.009 417	3.5×10^{-5}
2002dj	NGC 5018	0.009 375	35	0.009 400	0.009 37	5.1×10^{-6}
2002fk	NGC 1309	0.007 185	79	0.007 180	0.007 185	-4.4×10^{-7}
2002ha	NGC 6962	0.014 109	67	0.014 035	0.014 07	6.6×10^{-5}
2003ch	UGC 03787	0.028 702	17	0.028 890	0.028 62	8.2×10^{-5}
2003ic	MCG -02-02-086	0.055 435	31	0.055 340	0.055 359	7.6×10^{-5}
2003iv	UGC 02320 NOTES01	0.034 504	22	0.034 520	0.034 26	2.4×10^{-4}
2004dt	NGC 0799	0.019 505	19	0.019 550	0.019 418	8.7×10^{-5}
2004eo	NGC 6928	0.015 791	111	0.015 795	0.015 464	3.0×10^{-4}
2004ey	UGC 11816	0.015 832	13	0.015 750	0.015 834	-1.7×10^{-6}
2004gc	ARP 327 NED04	0.031 471	16	0.031 490	0.031 92	-4.5×10^{-4}
2005al	NGC 5304	0.012 454	12	0.012 480	0.0124	5.4×10^{-5}
2005am	NGC 2811	0.007 095	162	0.007 105	0.007 899	-8.1×10^{-4}
2005bo	NGC 4708	0.013 902	31	0.013 910	0.013 896	5.9×10^{-6}
2005cf	MCG -01-39-003	0.006 651	54	0.006 660	0.006 43	2.2×10^{-4}
2005el	NGC 1819	0.014 835	64	0.014 840	0.014 83	4.5×10^{-6}
2005eq	MCG -01-09-006	0.029 096	25	0.029 130	0.028 952	1.4×10^{-4}
2005ff	WISEA J223041.16-004634.2	0.089 810	1	0.089 690	0.089 79	2.0×10^{-5}
2005fn	SDSS J204853.04+001129.8	0.095 310	1	0.095 270	0.0951	2.1×10^{-4}
2005hj	WISEA J012648.45-011417.0	0.057 517	3	0.057 470	0.057 385	1.3×10^{-4}
2005iq	ESO 538- G 013	0.034 126	15	0.034 110	0.034 043	8.3×10^{-5}
2005kc	NGC 7311	0.015 125	35	0.015 090	0.015 09	3.5×10^{-5}
2005ki	NGC 3332	0.019 584	20	0.019 560	0.019 458	1.3×10^{-4}
2005kt ^a	WISEA J011058.06+001634.1	0.065 360	2	0.065 380	0.065 404	-4.4×10^{-5}
2005ku	WISEA J225942.70-000048.3	0.045 328	22	0.045 440	0.045 248	8.0×10^{-5}
2005lk	2MFGC 16592	0.104 400	1	0.104 220	0.104 161	2.4×10^{-4}
2005lu	ESO 545- G 038	0.032 091	22	0.032 080	0.032 189	-9.8×10^{-5}
2006al	WISEA J103928.52+051101.2	0.067 770	1	0.067 760	0.067 802	-3.2×10^{-5}
2006ax	NGC 3663	0.016 722	29	0.016 750	0.016 495	2.3×10^{-4}
2006bh	NGC 7329	0.010 894	27	0.010 900	0.010 767	1.3×10^{-4}
2006D	MRK 1337	0.008 491	169	0.008 433	0.008 53	-4.6×10^{-6}
2006ef	NGC 0809	0.017 959	14	0.017 940	0.017 812	1.5×10^{-4}
2006ej	NGC 0191A	0.020 439	18	0.020 360	0.020 38	5.9×10^{-5}
2006eq	2MASX J21283758+0113490	0.049 472	12	0.049 520	0.049 408	2.6×10^{-5}
2006et	NGC 0232	0.022 764	25	0.022 640	0.022 639	1.2×10^{-4}
2006fd	2MASX J20375343+0113100	0.079 965	21	0.080 035	0.079 948	5.3×10^{-5}
2006fy	WISEA J232640.11-005025.9	0.082 766	5	0.082 730	0.082 734	3.2×10^{-5}
2006gt	WISEA J005618.02-013730.9	0.044 810	4	0.044 710	0.044 799	1.1×10^{-5}
2006hb	ESO 552- G 052	0.015 141	43	0.015 140	0.014 957	2.1×10^{-4}
2006hx	2MASX J01135716+0022171	0.045 520	6	0.045 480	0.045 389	1.3×10^{-4}
2006is	WISEA J051734.55-234659.7	0.031 380	1	0.031 320	0.0314	-2.0×10^{-5}
2006kf	UGC 02829	0.021 533	25	0.021 540	0.020 037	1.5×10^{-3}
2006lu	WISEA J091517.24-253600.6	0.053 303	26	0.053 270	0.0534	-9.7×10^{-5}
2006oa	WISEA J212342.91-005034.7	0.062 510	2	0.062 505	0.062 573	-3.3×10^{-5}
2006on	WISEA J215558.50-010412.9	0.071 820	1	0.071 820	0.071 915	-9.5×10^{-5}
2006py	WISEA J224142.06-000812.7	0.057 855	2	0.057 930	0.057 866	1.0×10^{-4}
2007af	NGC 5584	0.005 482	29	0.005 500	0.005 524	-4.2×10^{-5}
2007al	WISEA J095918.72-192823.2	0.012 218	19	0.012 220	0.012 175	4.3×10^{-5}
2007as	ESO 018- G 018	0.017 098	43	0.017 140	0.017 572	-4.7×10^{-4}
2007bd	UGC 04455	0.031 035	25	0.031 100	0.030 44	6.0×10^{-4}
2007ca	MCG -02-34-061	0.014 104	32	0.014 100	0.014 066	3.8×10^{-5}

Redshift results. (continued)

SN	Host	$z_{\text{hel}}^{\text{WiFeS}}$	N_z	$z_{\text{hel,centre}}^{\text{WiFeS}}$	$z_{\text{hel}}^{\text{Pantheon+}}$	$z_{\text{hel}}^{\text{WiFeS}} - z_{\text{hel}}^{\text{Pantheon+}}$
2007cb	ESO 510- G 031	0.036 520	1	0.036 570	0.036 592	-7.2×10^{-5}
2007cc	ESO 578- G 026	0.029 051	14	0.029 040	0.029 125	-7.4×10^{-5}
2007cq	WISEA J221440.71+050442.3	0.025 927	26	0.025 840	0.026 04	-1.1×10^{-4}
2007fb	UGC 12859	0.017 990	23	0.017 920	0.018 026	-3.6×10^{-5}
2007ht	2MASX J00343398-0112577	0.072 853	3	0.073 040	0.072 753	1.0×10^{-4}
2007jh	CGCG 391-014	0.040 891	16	0.040 850	0.040 744	1.5×10^{-4}
2007ks	SDSS J204933.00-004543.0	0.096 845	2	0.096 855	0.098	-1.1×10^{-3}
2007le	NGC 7721	0.006 756	49	0.006 750	0.006 721	3.5×10^{-5}
2007nq	UGC 00595	0.045 223	32	0.045 150	0.045 21	3.1×10^{-5}
2007om	WISEA J235420.72-005501.0	0.105 160	1	0.105 330	0.104 84	3.2×10^{-4}
2007on	NGC 1404	0.006 451	76	0.006 460	0.006 248	2.0×10^{-4}
2007pu	SDSS J224558.32-003855.9	0.091 350	1	0.091 360	0.0914	-5.0×10^{-5}
2007ra	WISEA J233424.11-005324.7	0.089 158	6	0.089 290	0.089 163	-4.7×10^{-6}
2007sr	NGC 4038	0.005 550	96	0.005 640	0.005 417	1.3×10^{-4}
2007st	NGC 0692	0.021 252	31	0.021 250	0.021 181	7.1×10^{-5}
2008051	GALEXASC J151958.89+045417.3	0.037 960	1	0.038 010	0.037 77	1.9×10^{-4}
2008ar	IC 3284	0.026 252	14	0.026 230	0.026 173	7.9×10^{-5}
2008bc	KK 1524	0.014 828	40	0.014 825	0.015 087	-2.7×10^{-4}
2008bi	NGC 2618	0.013 532	33	0.013 630	0.013 456	7.6×10^{-5}
2008bq	ESO 308- G 025	0.034 448	22	0.034 440	0.034 007	4.4×10^{-4}
2008cc	ESO 107- G 004	0.010 475	59	0.010 465	0.010 304	2.0×10^{-4}
2008cf	LEDA 766647	0.047 290	1	0.047 250	0.046 03	1.3×10^{-3}
2008ff	ESO 284- G 032	0.019 165	2	0.019 170	0.019 249	-7.9×10^{-5}
2008fl	NGC 6805	0.020 231	41	0.020 210	0.019 88	3.8×10^{-4}
2008fr	LEDA 5069093	0.039 500	1	0.039 480	0.039	5.0×10^{-4}
2008fu	ESO 480-IG 021	0.052 121	29	0.052 280	0.052 016	1.0×10^{-4}
2008fw	NGC 3261	0.008 522	79	0.008 600	0.008 379	1.4×10^{-4}
2008gg	NGC 0539	0.032 091	18	0.032 070	0.032 025	6.6×10^{-5}
2008gl	UGC 00881	0.034 226	15	0.034 220	0.0342	2.6×10^{-5}
2008go	WISEA J221043.94-204725.9	0.062 215	11	0.062 125	0.062 273	-1.7×10^{-4}
2008gp	MCG +00-09-074	0.033 144	17	0.033 170	0.0335	-3.6×10^{-4}
2008hj	MCG -02-01-014	0.037 609	41	0.037 680	0.037 613	-3.7×10^{-6}
2008hu	ESO 561- G 018	0.049 940	11	0.050 040	0.049 698	2.4×10^{-4}
2008hv	NGC 2765	0.012 743	107	0.012 755	0.012 549	1.8×10^{-4}
2008ia	ESO 125- G 006	0.022 054	85	0.022 020	0.021 942	1.0×10^{-4}
2008Q	NGC 0524	0.008 129	66	0.008 150	0.008 016	1.1×10^{-4}
2008R	NGC 1200	0.013 494	42	0.013 490	0.013 296	2.0×10^{-4}
2009aa	ESO 570- G 020	0.027 383	25	0.027 380	0.027 052	3.3×10^{-4}
2009ab	UGC 02998	0.011 102	25	0.011 120	0.011 178	-7.6×10^{-5}
2009ad	UGC 03236	0.028 356	21	0.028 400	0.0284	-4.4×10^{-5}
2009ag	ESO 492- G 002	0.008 731	67	0.008 740	0.008 686	4.5×10^{-5}
2009al	NGC 3388	0.022 063	17	0.022 090	0.022 069	-6.1×10^{-6}
2009ds	NGC 3905	0.019 188	19	0.019 060	0.019 09	9.8×10^{-5}
2009D	ESO 549- G 031	0.025 100	42	0.025 250	0.025 097	2.5×10^{-6}
2009ig	NGC 1015	0.008 825	33	0.008 820	0.008 77	5.5×10^{-5}
2009kk	2MFGC 03182	0.012 505	17	0.012 620	0.012 859	-3.5×10^{-4}
2009le	ESO 478- G 006	0.017 855	55	0.017 870	0.018 149	-2.9×10^{-4}
2009Y	NGC 5728	0.009 486	87	0.009 635	0.009 743	-1.2×10^{-4}
2010A	UGC 02019	0.020 815	54	0.020 860	0.020 755	6.0×10^{-5}
2010H	IC 0494	0.015 257	31	0.015 390	0.015 197	6.0×10^{-5}
2013go	...	0.073 200	1	0.073 180	0.074	-8.0×10^{-4}
420100	WISEA J221225.27+005105.3	0.097 830	1	0.097 690	0.097 621	2.1×10^{-4}
530086	2MASX J22112814-0001456	0.051 690	1	0.051 950	0.052 003	-3.1×10^{-4}
ASASSN-15bc	LEDA 170061	0.036 928	18	0.036 850	0.036 715	2.1×10^{-4}
ASASSN-15hg	CGCG 063-098	0.030 056	19	0.029 980	0.029 917	1.4×10^{-4}
ASASSN-15il	2MASX J15570808-1240252	0.023 388	19	0.023 350	0.023 316	7.2×10^{-5}
ASASSN-15lg	CGCG 044-042	0.020 127	32	0.020 180	0.020 151	-2.3×10^{-5}
ASASSN-15nr	CGCG 082-031	0.023 168	25	0.023 150	0.023 206	-3.8×10^{-5}
ASASSN-15od	MCG -01-07-004	0.017 637	55	0.017 580	0.017 603	3.4×10^{-5}
ASASSN-15pr	2MASX J23063962-1234238	0.033 301	17	0.033 300	0.033 093	2.1×10^{-4}
ASASSN-15ss	MCG -02-16-004	0.035 624	27	0.035 700	0.035 558	6.6×10^{-5}
ASASSN-15uw	2MASX J02353437-0603496	0.030 388	12	0.030 320	0.030 811	-4.2×10^{-4}
ASASSN-16aj	NGC 1562	0.030 620	22	0.030 630	0.030 745	-1.2×10^{-4}
ASASSN-16ay	UGC 03738	0.028 306	24	0.028 290	0.028 343	-3.7×10^{-5}
ASASSN-16bc	2MASX J12052488-2123572	0.032 003	19	0.031 970	0.031 939	6.4×10^{-5}
ASASSN-16bq	IC 0986	0.024 988	25	0.024 990	0.024 935	5.3×10^{-5}
ASASSN-16br	2MASX J15453055-1309057	0.028 661	26	0.028 700	0.028 52	1.4×10^{-4}

Redshift results. (continued)

SN	Host	$z_{\text{hel}}^{\text{WiFeS}}$	N_z	$z_{\text{hel,centre}}^{\text{WiFeS}}$	$z_{\text{hel}}^{\text{Pantheon+}}$	$z_{\text{hel}}^{\text{WiFeS}} - z_{\text{hel}}^{\text{Pantheon+}}$
ASASSN-16ct	SDSS J151354.30+044525.7	0.041 910	1	0.041 910	0.041 91	0.0
ASASSN-16dn	GALEXASC J104848.62-201544.1	0.012 920	1	0.012 920	0.012 85	7.0×10^{-5}
ASASSN-16dw	2MASX J13300119-2758297	0.034 638	14	0.034 610	0.034 657	-1.9×10^{-5}
ASASSN-16fo	2MASX J13323577-0516218	0.029 234	9	0.029 250	0.0289	3.3×10^{-4}
ASASSN-16hz	2MASX J23154564-0120135	0.025 443	17	0.025 410	0.025 308	1.3×10^{-4}
ASASSN-16ip	ESO 479- G 007	0.017 167	19	0.017 180	0.017 008	1.6×10^{-4}
ASASSN-16jf	UGCA 430	0.011 440	12	0.011 390	0.011 441	-1.0×10^{-6}
ASASSN-16lg	ARK 530	0.021 367	41	0.021 380	0.021 171	2.0×10^{-4}
ASASSN-16oz	GALEXASC J090013.19-133803.5	0.030 150	1	0.030 110	0.031	-8.5×10^{-4}
ASASSN-17aj	MCG -02-30-003	0.021 444	20	0.021 420	0.021 275	1.7×10^{-4}
ASASSN-17co	UGC 11128	0.018 357	35	0.018 290	0.018 259	9.8×10^{-5}
AT2016aj	2MASX J04422451-2143312	0.067 430	1	0.067 460	0.067 406	2.4×10^{-5}
AT2016htm	2MASX J02320134-2639576	0.043 226	12	0.043 360	0.043 313	-8.7×10^{-5}
AT2016htn	2MASX J02112819-1630409	0.053 106	17	0.053 110	0.053 117	-1.1×10^{-5}
AT2017cfc	UGC 08783	0.023 840	1	0.023 820	0.024 027	-1.9×10^{-4}
AT2017lm	2MASX J03013238-1501028	0.030 449	21	0.030 440	0.030 636	-1.9×10^{-4}
AT2017ns	2MASX J02491020+1436036	0.029 373	11	0.029 370	0.028 766	6.1×10^{-4}
AT2017yk	2MASX J09443215-1218233	0.046 670	14	0.046 760	0.046 439	2.3×10^{-4}
AT2017zd	2MASX J13324217-2148034	0.029 486	14	0.029 650	0.029 47	1.6×10^{-5}
ATLAS16dpb	CGCG 415-040	0.022 781	22	0.022 790	0.023 083	-3.0×10^{-4}
ATLAS16dqf	WISEA J210907.40-180607.8	0.021 049	11	0.021 095	0.021 17	-1.5×10^{-4}
ATLAS17ajn	ESO 440- G 001	0.028 725	13	0.028 820	0.028 706	1.9×10^{-5}
ATLAS17axb	GALEXASC J134322.97-195637.5	0.031 580	1	0.031 630	0.031 652	-7.2×10^{-5}
Gaia16agf	...	0.025 285	13	0.025 320	0.025 066	2.2×10^{-4}
MASTERJ0134	GALEXASC J013415.00-174836.1	0.044 895	10	0.044 820	0.044 846	4.9×10^{-5}
MASTEROTJ08	2MASX J08325728-0351295	0.030 521	18	0.030 570	0.030 584	-6.3×10^{-5}
080064	GALEXASC J032942.01-275237.5	0.066 290	1	0.066 050	0.066 129	1.6×10^{-4}
100405	...	0.103 453	11	0.103 480	0.1034	5.3×10^{-5}
PS15aai	CGCG 071-025	0.046 510	23	0.046 500	0.046 549	-3.9×10^{-5}
PS15bif	...	0.079 633	3	0.079 673	0.079 37	2.3×10^{-4}
PS15bjg	2MASX J22551005-0024333	0.068 987	8	0.069 020	0.068 888	9.9×10^{-5}
PS15brr	GALEXASC J235326.18-153921.5	0.052 845	4	0.052 950	0.051 804	1.0×10^{-3}
PS15bsq	MCG -02-60-012	0.034 330	63	0.034 420	0.034 304	-1.7×10^{-5}
PS15cku	2MASX J01242239+0335168	0.023 446	15	0.023 460	0.023 273	1.7×10^{-4}
PS15cms	2MASX J09583540+0044336	0.064 884	18	0.064 860	0.064 79	9.4×10^{-5}
PS15coh	GALEXASC J021558.44+121415.2	0.019 027	4	0.019 040	0.018 837	1.9×10^{-4}
PS15cwx	2MFGC 04279	0.030 310	1	0.030 280	0.030 065	2.4×10^{-4}
PS15cze	2MASX J03472342+0052316	0.039 421	9	0.039 420	0.039 371	5.0×10^{-5}
PS16axi	2MASX J10480747+0010017	0.039 333	15	0.039 440	0.039 299	3.4×10^{-5}
PS16ayd	2MASX J14271887-0140428	0.054 097	7	0.053 910	0.053 997	1.0×10^{-4}
PS16bby	2MASX J14201699-2211186	0.053 550	24	0.053 570	0.053 427	1.2×10^{-4}
PS16bnz	UGC 05586 NED02	0.062 893	31	0.062 860	0.0627	1.6×10^{-4}
PS16cqa	2MFGC 12594	0.043 944	30	0.044 060	0.043 857	7.8×10^{-5}
PS16em	LCRS B105301.1-030602	0.069 997	8	0.070 100	0.069 815	1.8×10^{-4}
PS16evk	2MASX J22323338-0121266	0.054 530	1	0.054 550	0.054 468	6.2×10^{-5}
PS16fa	CGCG 036-091	0.046 043	40	0.046 170	0.046 11	-6.7×10^{-5}
PS16fbb	GALEXASC J000703.01-204149.5	0.052 183	12	0.052 240	0.0525	-3.2×10^{-4}
PS17akj	LCRS B134713.8-024957	0.046 688	9	0.046 770	0.046 808	-1.2×10^{-4}
PS17bii	2MASX J11253836+0720042	0.073 406	10	0.073 500	0.073 391	1.5×10^{-5}
PSNJ2043531	NGC 6956	0.015 513	43	0.015 540	0.015 497	1.6×10^{-5}
360156	WISEA J100313.52+015343.0	0.045 598	43	0.045 560	0.045 507	9.1×10^{-5}
PTSS-16efw	2MASX J17353788+0848387	0.036 146	19	0.036 230	0.035 573	5.7×10^{-4}
SN2016gmb	GALEXASC J003445.02-060936.8	0.058 125	4	0.058 160	0.058 269	-1.4×10^{-4}
SN2016hpx	2MASX J0603164-265353	0.031 831	16	0.031 770	0.033 375	-1.5×10^{-3}
SN2017cvj	LCRS B100813.8-033156	0.059 512	4	0.059 580	0.059 528	-1.6×10^{-5}
SN2017hn	UGC 08204	0.023 897	23	0.023 810	0.023 85	4.7×10^{-5}

^a SN 2005kt was in Pantheon, but not Pantheon+ as the Type Ia classification is not secure (Sako *et al.*, 2018; Carr *et al.*, 2022). Thus, the reference redshift is actually from the NASA/IPAC Extragalactic Database.